UNIVERSITÀ DELLA CALABRIA

UNIVERSITA' DELLA CALABRIA

Dipartimento di FISICA

Dottorato di Ricerca in

FISICA

Con il contributo di (Ente finanziatore)

Fondo Sociale Europeo

CICLO

XXVII

ATOMIC FORCE MICROSCOPY OF CORNEAL BIOMECHANIC

Settore Scientifico Disciplinare FIS/07

Coordinatore: Prof. CARLO VERSACE

Firma _____

Supervisori: Dott.ssa MARIA PENELOPE DE SANTO

Firma _____

Prof. RICCARDO BARBERI

Firma _____

Dottorando: Dott./ssa CRISTINA LABATE

Firma _____

UNIVERSITÀ DELLA CALABRIA

UNIVERSITA' DELLA CALABRIA

Dipartimento di FISICA

Scuola di Dottorato

SCIENZEA E TECNICA "BERNARDINO TELESIO"

Indirizzo

FISICA

MATERIALI MOLECOLARI E MESOFASI

Con il contributo di (Ente finanziatore)

Fondo Sociale Europeo

CICLO

XXVII

ATOMIC FORCE MICROSCOPY OF CORNEAL BIOMECHANIC

Settore Scientifico Disciplinare FIS/07

Coordinatore: Prof. CARLO VERSACE

Firma

Supervisori: Dott.ssa MARIA PENELOPE DE SANTO

Firma

Prof. RICCARDO BARBERI

Firma

Dottorando: Dott./ssa CRISTINA LABATE

Firma

ATOMIC FORCE MICROSCOPY OF CORNEAL BIOMECHANICS

Thesis by

CRISTINA LABATE

In Partial Fulfillment of the

Requirements

for the Degree of

Doctor of Philosophy

University of Calabria

January 2015

To my family

Acknowledgements

First and foremost I want to thank my supervisor Dr. Maria Penelope De Santo. It has been an honor to be her first Ph.D. student. She has taught me, both consciously and unconsciously, how good experimental physics is done. I appreciate all her contributions of time, ideas, and funding to make my Ph.D. experience productive and stimulating. The joy and enthusiasm she has for her research was contagious and motivational for me, even during tough times in the Ph.D. pursuit. I am also thankful for the excellent example she has provided as a successful woman physicist and professor.

I am also thankful to my second supervisor, Prof. Riccardo Barberi, he was so kind to me and he never ever hesitated to help me when I asked him. I will never forget his smile and his friendly personality.

This thesis could not have been written without the support, encouragement and help of Dr. Giuseppe Lombardo and Dr. Marco Lombardo. The members of the LiCryl group have contributed immensely to my personal and professional time at UniCal. The group has been a source of good advice and collaboration. I am grateful to Dr. Bruno Zappone, Dr. Rita Guzzi and Dr. Bruno Rizzuti.

I extend a big thank you also to Prof. Ziebarth for providing me with this extraordinary opportunity to research within her laboratory at the University of Miami.

I also would like to thank the European Social Fund (FSE) and Department of Physics for funding support.

Lastly, I would to like to acknowledge my parents, Swami (mom) and Sosan (dad), for rais-

ing me, for bearing with me during the challenges, and for joining me in the triumphs, for letting me be a bit too ridiculous occasionally when my passions led me there, for never damping my sense of curiosity, for never imposing, for never having anything but confidence in me. For the presence of my brother Luca, my life partner.

And most of all for my loving, supportive, encouraging, and patient boyfriend Giuseppe whose faithful support during the final stages of this Ph.D. is so appreciated.

Thank you.

Contents

Introduction

The human eye is the organ which allows us to see and interpret the shapes, colors, and dimensions of objects by processing the light they reflect or emit. The cornea is the transparent front part of the eye that covers the iris, pupil, and anterior chamber and that provides 2/3 of the eye's focusing power. The cornea has the structure of a thin shell with the external and internal surfaces described by ellipsoids. The average in plane diameter is 12 ± 1 mm; the radii of curvatures for the exterior and interior surfaces are different, as a consequence of the variable thickness, the cornea is thinner centrally (averagely 520 μm) than peripherally (av. 650 μm). The corneal tissue is organized in five layers, which are parallel to the external surface: epithelium, Bowman's layer, stroma, Descemet's membrane, endothelium. The stroma accounts for 90% of the corneal thickness, it is organized in about 300-500 collagen lamellae, composed of bundles of collagen fibrils surrounded by a jelly like matrix mostly made by proteoglycans.

In the past decades the importance of corneal biomechanics in the normal and pathological functions of the eye has gained its credibility. In fact, the mechanical properties of biological tissues are essential to their physiological function. Understanding the biomechanics of the corneal tissue is a keystone for the care of eye diseases. The vast majority of the researches on corneal mechanics are focused on the macroscopic, overall mechanical properties of corneal tissue, without considering the molecular nanoscale structure. We are convinced that an improved understanding of the nanomechanics of corneal tissue is important to enlighten the basic molecular interactions between collagen fibrils and may ultimately help in the development of new techniques to cure ocular diseases. Nanotechnology techniques can give us new and deeper information on the mechanics of the cornea, allowing us to design accurate model for the description of the mechanical behaviour of the corneal tissue.

Atomic Force microscopy has become popular in biomedical sciences as a tool for investigating topographical and mechanical properties of biological and biosynthetic materials at

the nanoscale. In fact, the technique allows either to image features or to probe the elasticity of materials that are soft and exhibit inhomogeneity with nanometer scale resolution. Indentation using the atomic force microscope is evolving as a powerful tool for investigating the regional micro- and submicro-mechanical properties of a variety of biological tissues and biomaterials close to their native conditions.

The research presented in this thesis is focused mainly on the study of the mechanical properties of the corneal stroma using atomic force microscopy. This work is framed in the research program of the National project PON-Nanoftalm, that aims to study new nanotechnological platforms for drug delivery in Ophthalmology.

The first part of our research was devoted to the study of the effects induced in corneal tissues by the riboflavin/UV-A cross-linking technique, used for the treatment of the corneal disease known as keratoconus. The thinning and weakening of the cornea in this disease causes the cornea to bulge out under normal intraocular pressures. With increasing degrees of protrusion, correction by spectacles and contact lens wear becomes more and more difficult. Eventually 20% of patients require corneal transplantation because refractive correction is no longer possible. The use of riboflavin activated by ultraviolet light and the use of crosslinkers to treat tissue works on the presupposition that by increasing the strength and mechanical stability of the tissue, the disease progression may be halted. Studies in vitro indicate that crosslinking can improve tissue mechanical stability and resistance to deformation. Our research was aimed to obtain quantitative information on the improvement of the corneal stability following keratoconus at the molecular level. All the research was carried out on human donor corneas, and the results have provided the first evidence that riboflavin/UV-A corneal cross-linking induces both an increase of the elastic response and a decrease of the viscous response of the stroma at the scale of stromal molecular interactions. The results are consistent with the knowledge that the formation of additional cross-linking bonds may occur at preferred sites of the surface of stromal collagen fibrils and proteoglycan core proteins.

The second part of the research was carried out at the Department of Biomedical Engineering, University of Miami, USA. The aim of the study was to investigate the depth-dependent mechanical anisotropy of the human corneal stroma at the micro- and nano-level and to determine whether the biomechanics of the stroma involves any relationships between different scales of measurement. All the performed research was carried out on human donor corneas. At all scales, increasing the stromal depth has resulted in a decrease of the elastic properties of the stroma. Further, we have the first evidence that the observed decrease takes place in

different ways when we probe at the single fibril level or on a micrometer size area. The results are consistent with the notion that the anterior stroma is less hydrated than the posterior stroma and appears to be stiffer than the latter with stronger links between collagen lamellas. Interlamellar cross-links, which are preferentially distributed in the anterior one third and periphery of the stroma contribute to the regional differences in lamellar shearing strength and interlamellar cohesive strength in the human cornea.

This thesis is structured as follows:

in Chapter 1 is provided a general picture of the anatomy and physiology of the eye, together with a description of the keratoconus disease. Then, a brief description of corneal cross linking is provided;

in Chapter 2 is given an introduction on contact mechanics;

in Chapter 3 are described the materials and experimental methods used for the research. In particular, atomic force microscopy as investigation technique is introduced in detail;

in Chapter 4 the study on the viscoelastic response of the human corneal stroma following riboflavin/UV-A cross-linking treatment at the nano-level is presented;

in Chapter 5 the study on the depth-dependent mechanical anisotropy of corneal stroma is presented;

Chapter 1

ANATOMY AND PHYSIOLOGY OF THE EYE

1.1 The Physiology of the Eye

Vision is a complex process which depends on many processes that must work together. The human eye consists of very precise parts, and each part has a different function. The major constituents of the eye are shown in figure 1.1 (a).

Cornea is one of the principal optical components [1] (Fig 1.1 b,c); it constitutes the outer part of the front of the eye, and provides 2/3 of the eye's optical power. It is surrounded by fluid anteriorly (tear film) and posteriorly (aqueous humour), and is composed of clear transparent tissue. There are no blood vessels in the cornea; however, it is extremely sensitive because there are many nerve endings [3].

The focusing of the light is accomplished mainly by the cornea, by the fact that it has a curved surface which "bends" the light.

The overall ocular refractive power of the eye is around 60 diopters, which comes from the cornea and the crystalline lens. In the young eye the crystalline lens has the capability to reshape upon an accommodating stimulus and contributes with a dioptric power between around 14 D (relaxed accommodation) to 37 D (maximally accommodated) [5]. The flexibility of the lens decreases with age and, hence, the ability of accommodation is lost (known as Presbyopia). A variable aperture (the iris) is placed between the cornea and the lens, contracting

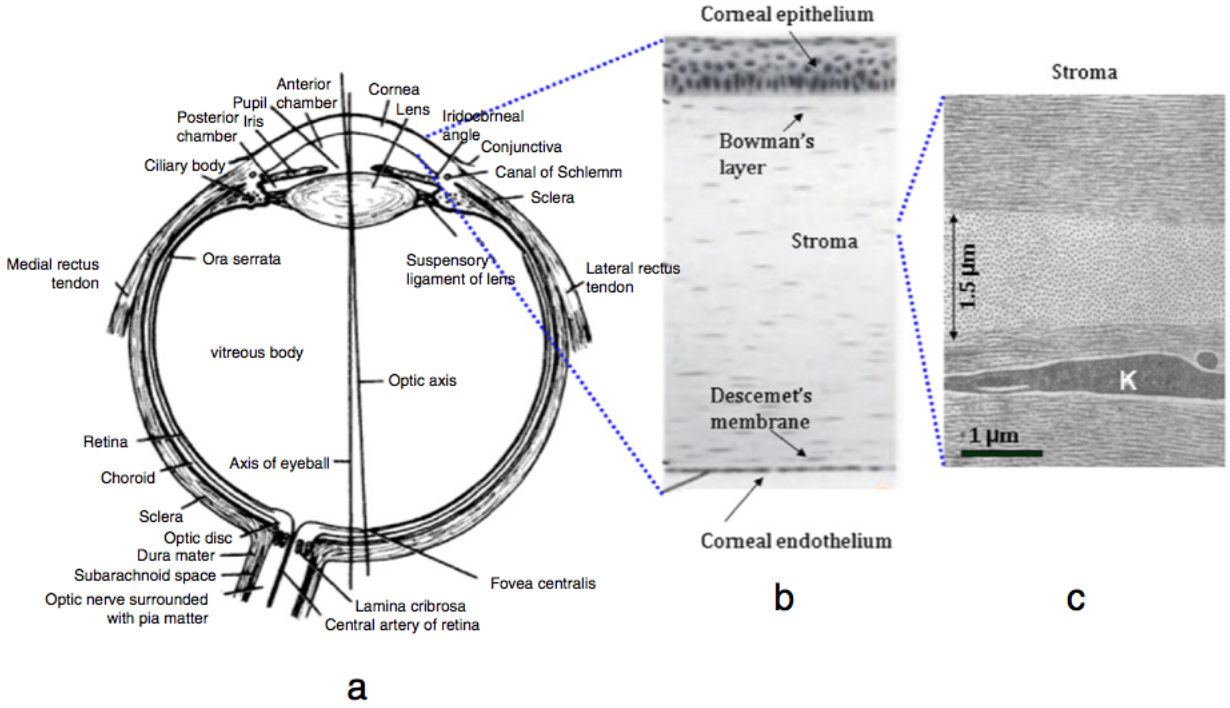

Figure 1.1: (a) Cross-section of the human eye. (b) Expanded view of the cornea showing the five layers: epithelium, Bowman's layer, stroma, Descemet's membrane, and endothelium. (c) TEM image of the stroma in the cornea showing two preferred orientations of collagen fibrils in successive lamellae. K: Keratocytes. [2]

upon increased illumination. This aperture (pupil) controls the amount of light that enters the eye and plays a significant role in image quality. The medium between cornea and lens is called the aqueous humor (anterior chamber), the medium between lens and retina is the vitreous humor. Both humors consist primarily of H_2O and provide the necessary pressure to maintain the shape of the ocular coat (cornea, limbus, sclera) and the lens position. Typical dimensions of the human eye globe are: 21-27 mm axial length, 23 mm vertical diameter, 23.5 mm horizontal diameter. Before introducing the corneal structure, we will briefly introduce the different types and structure of collagen fibrils. Collagen fibrils are the main constituents of the corneal tissue.

1.2 Collagen

Collagen is among the most important structural proteins. The word collagen is derived from Greek word *kallagene*, which means *glue forming*. There are over 25 different types of collagen which are a major component in Extra-Cellular Matrices (ECMs) and they are categorized by Roman numerals (collagen type I, II, III...). Of these, five *fibril forming* collagens have been detected (I, II, III, V, XI) in connective tissue such as Ligaments, Tendons and Cornea. Different connective tissues have their own specific microscopic and macroscopic structural appearances which are completely adapted with their functions and performances (i.e. transparency in cornea, tensile bearing in tendon and load-bearing in bone). Collagens are very important in ECMs since they provide mechanical strength and flexibility of tissue and also promote cell growth. Collagen molecules are adapted to carry tensile loads along their principal axis and are thus anisotropically arranged into aligned fibrils in load-bearing ECMs. There is little information available about how collagenous tissue organization is generated and maintained during development and growth [6]. However, it has been presumed that mechanical load plays a critical role in epigenetic regulation of load-bearing collagenous ECMs [6]. Collagen type I is the most abundant type of fibrils in connective tissue (and is consequently the most observed) [7]. It forms over 80% of collagenous structures in all ECMs. It is the principal determinant of load-bearing matrix mechanical properties and plays a crucial role in mechanical behavior [8]. The aminoacid composition of collagen is atypical for proteins, particularly with respect to its high hyohoxyproline content. The basic structure of collagens at the supramolecular level is a right-handed, linear, triple helix comprising three left-handed helical alpha chains to form

a rope-like molecule (Fig. 1.2 a). The chemical structure of each collagen molecule is named αA, αB and αC and consists of sequential chains of the Glycine-X-Y which are repeated in the special form of (Gly-X_{aa}-Y_{aa}) in which, X_{aa} and Y_{aa} are typically Proline and Hydroxyproline. Glycine is the smallest amino acid found and is every third residue (Fig. 1.2 b) [9].

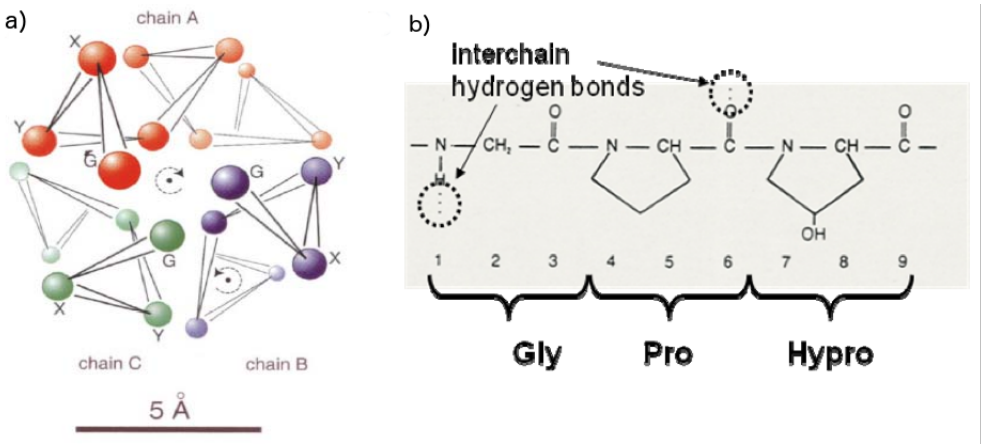

Figure 1.2: a) Triple-helix of three left-handed helical chains. b) Each chain consists Glycine (Gly- X-Y repeats where X and Y are generally pro- or hypro-) repeating triplet of amino acid residues [9]

this structure is called pro-collagen and it (fig 1.3 a) is 300 nm long, 1.5 nm wide. The pro-collagen is the building block of collagen fibers. Pro-collagen chains are synthesized by cells and are brought together by C-propeptides and generate a triple-helical molecule known as pro-collagens trimer fig 1.3 c. This trimer is comprised of three parts (N-proteinase, collagen and C-proteinase). The C-propeptide is at one end of the pro-collagen molecule and the N-propeptide is at the other end. Pro-collagen is subjected to proteinase enzymes which cleave N- and C- terminals from procollagen and convert it to tropo-collagen fig 1.3 d. Without these enzymes the formation of fibrils would not occur. After this process, collagen monomer, usually about 42 nm in length, is ready to combine with other collagen monomers fig 1.3 e.

The assembly of collagen monomers into fibrils is an entropy driven process [7]. These processes are driven by the loss of solvent molecules from the surface of proteins and result in assembled fibrils with a circular cross-section, which minimizes the surface area volume ratio of the final assembly. Although the broad principles of collagen fibril self-assembly are generally accepted, less is known about the molecular mechanisms of the assembly process. Fibril formation is controlled to a large extend by the amino acid sequence of the collagen monomer and, in particular, by the distribution of polar and hydrophobic residues that are exposed on

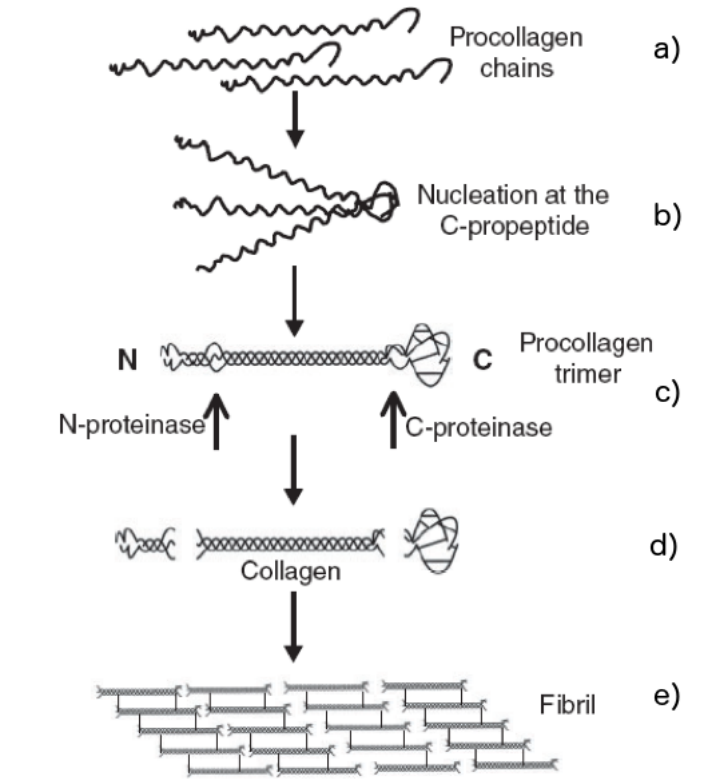

Figure 1.3: Overview of collagen fibrils formation. Procollagen chains are brought together to form a rod-like triple helical domain. Then, N- and C- terminals are removed from the procollagen in order to assemble into fibrils [10]

the surface of the triple helix. In fig. 1.6a a stretch the Smith model for collagen fiber formation is shown. In this model, five collagen type I molecules are assembled to each other to form a collagen micro-fibril. The exact mode of organization of the collagen molecules in the microfibrils and their exact number, is still a subject for speculation. The fibrils are stabilized by covalent cross-link bonds, which is initiated by oxidative deamination of specific lysine and hydroxy lysine residues in collagen molecules by lysyl oxidase. Experiments have also highlighted that micro-fibrils spontaneously self-assemble with regularly staggered ends (fig.1.4).

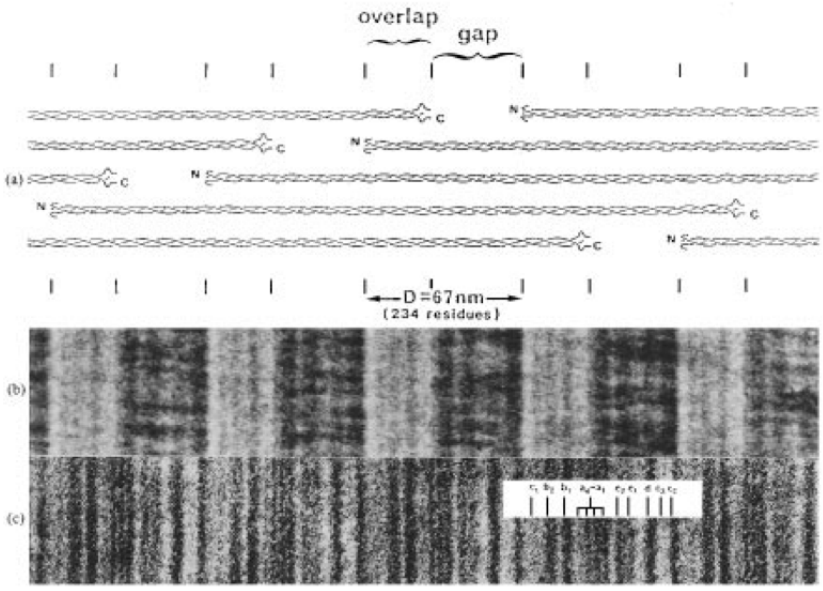

Figure 1.4: Axial structure of D-periodic collagen fibrils. (a) Schematic representation of the axial packing arrangement of triple-helical collagen molecules in a fibril, as derived from analysis of the positive (c) and negative (b) staining patterns. (b) Collagen fibril negatively stained with sodium phosphotungstic acid (1%, pH 7). The fibril is from a gel of fibrils reconstituted from acetic-acid-soluble calf-skin collagen. The repeating broad dark and light zones are produced by preferential stain penetration into regions of lowest packing (the gap regions). (c) Similar fibril positively stained with phosphotungstic acid (1%, pH 3.4) and then uranyl acetate (1%, pH 4.2). The darkly staining transverse bands are the result of uptake of electron-dense heavy-metal ions from the staining solutions on to charged residue side groups of collagen.[7]

The diameter of micro-fibrils is 4 nm which is the minimum diameter for filamentous structure that possesses an axial D repeat. This assembly of collagen micro- fibrils generates the formation of larger fibrils, through end to end as well as lateral aggregation. The D-stagger

of collagen molecules produces alternating regions of protein density in the fibrils which explains the characteristic periodicity in AFM and TEM images [11] (fig. 1.5).

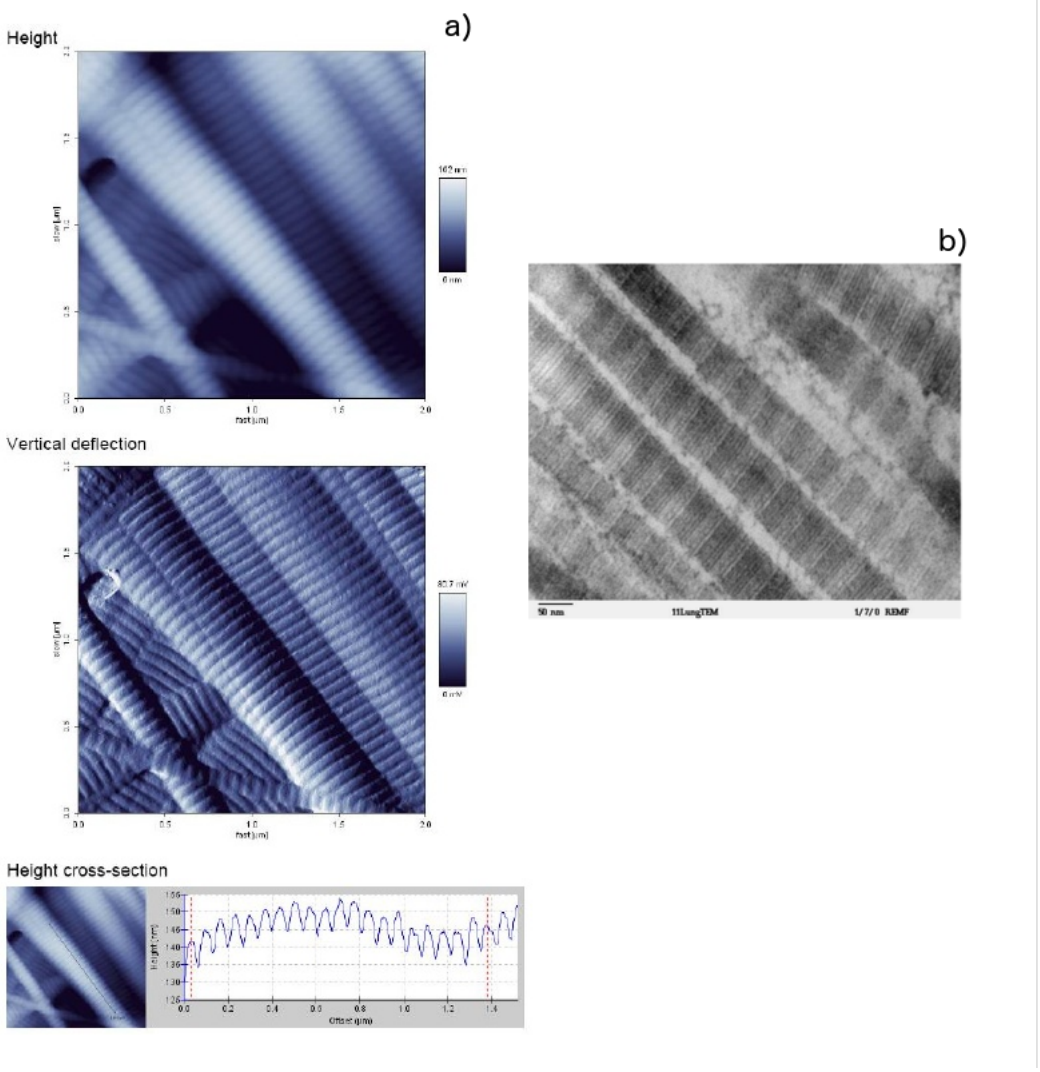

Figure 1.5: Characteristic periodicity in the fibrils is shown in the AFM (a) and TEM images (b).

Examining the radial section of the collagen fiber (fig. 1.6b) the periodic distribution of the single collagen molecules, is highlighted (fig. 1.6.b,c). The diameter of fibrils ranges from 30nm to 500nm and depends on tissue, age and genetics. In other words, the diameter and formation of fibrils from micro-fibrils are completely different in different kinds of tissue. In cornea, fibrils are arranged in multiple layers or lamella. Each layer is comprised of aligned fibrils. Between layers, there is a constant angular twist (often 90°) which results in a plywood-

like arrangement [11].

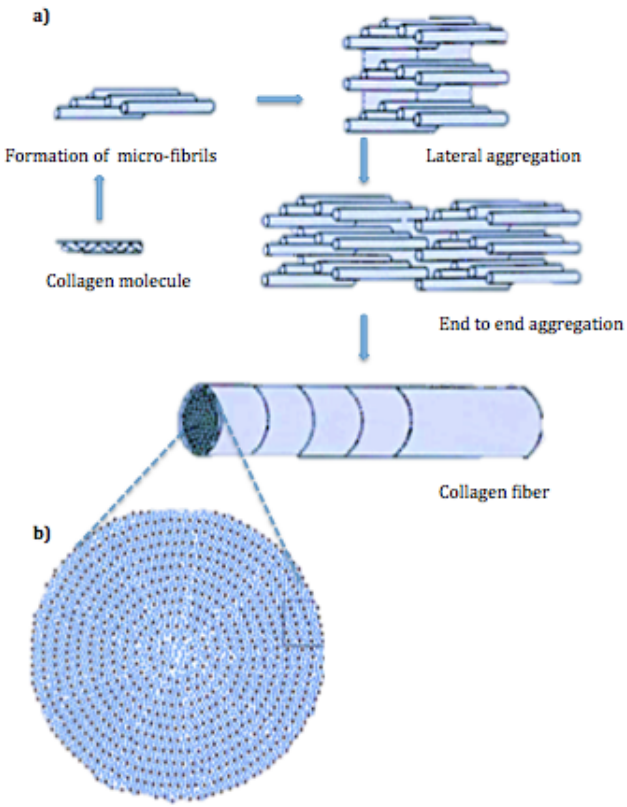

Figure 1.6: a) Schematic of assembly micro-fibrils into the fibril. b) Sectionof radial packing of collagen molecules[11].

1.3 Stromal Collagen

Corneal collagen fibrils are 25-30nm in diameter [12]. Stromal collagen differs from the one in other connective tissues, such as the collagen fibrils in the sclera, which have a non-uniform diameter from 25 to 230nm. The narrow, uniform collagen fibrils give the cornea its clarity, because they run parallel to each other. The spacing of the fibrils is another essential factor in maintaining the transparent nature of the cornea [1]. When the distance between the collagen fibrils or between the lamellae increases the cornea loses some of its transparency

[13]. The perfect transparency depends on the presence of stromal proteoglycans that associate with collagen fibrils. Proteoglycans are glyco-proteins, which have linear side chains of negatively changed disaccharide units called glycosaminoglycans (GAGs) that are bound covalently at one end to a PG care protein, which in turn is attached to a collagen fibril. The charged GAG chains interact electrostatically with ions in the inter fibrillar fluid to produce osmotic pressure. Recent works show that GAG chains do appear to form bridging structures between two or more fibrils. Though interactions with collagen, PG with the GAGs help define the hydrophilicity and swelling properties of the corneal matrix as well as the spatial organization of the collagen fibers [14].

1.4 General Structure and Function of the Cornea

The cornea forms the outer shell of the anterior eye ball with highly organized collagen fibrils, which gives the avascular tissue a high transparency [15]. Both, the diameter of and the distance between individual collagen fibers is less than half of the wavelength of visible light, and therefore scattering on individual fibers gets canceled out by destructive interference. If this equilibrium is disturbed the cornea gets opaque (e.g., fibril swelling due to hydration etc.). Being exposed to the environment on one side, the cornea as well as the sclera serve to protect the inner eye components. Thereby the combination of high rigidity and viscoelasticity allows absorbing physical injury (strokes etc.) and at the same time maintaining the ocular shape. The last one is especially important as the corneal refraction is very sensitive to small changes in corneal shape, smoothness and thickness which quickly can cause visual distortion. The corneal surface of an adult human is aspheric and convex. The cornea measures 11 to 12 mm in the horizontal diameter, 9 to 11 mm in the vertical diameter and its thickness shows a gradient increasing gradually from the center 520 μm to the periphery 670 μm. Population average values for the radius of curvature is 7.8 mm for the anterior surface and 6.5 mm for the posterior surface. Externally the cornea is covered by the tear-film that helps maintaining a smooth surface. Interiorly the cornea is in touch with the aqueous humor getting provided with nutrients. The cornea consists of three cellular layers and two membranes which are explained in more detail below:

Corneal Layers

EPITHELIUM The epithelium is the outermost layer and consists of non-keratinized stratified squamous epithelial cells. It is made of about six cell layers and has a thickness of about 50 μm. Epithelial cells proliferate from stem cells in the limbus and grow very fast. It takes a few days to recover after epithelial abrasion. Primarily the epithelium controls corneal hydration from the anterior side by preventing liquids to enter into the stroma. The epithelium also contributes to establish a smooth anterior surface. Irregularities lead to an alteration of the tear-film causing a significant alteration of corneal refraction. Only a negligible contribution to corneal stiffness is attributed to the epithelium [17].

BOWMAN' S LAYER The Bowman' s layer is a non-cellular layer of about 8-14 μm thickness and consists of condensed and irregularly arranged collagen type I (primarily) and III fibrils. Although the type of collagen fibrils is the same as in the stroma, the fiber diameter in the Bowman' s layer is slightly smaller (20 to 30 μm). Due to its higher stiffness, the Bowman' s layer protects the corneal stroma. It does not recover after rupture and is absent in most non-primates.

STROMA The stroma makes out the largest part of the cornea (about 90%) and therefore most biomechanical properties of the cornea are determined by this layer. The stroma is composed of an extracellular matrix, keratocytes (fibroblasts) and nerve fibers. About 70% of the dry weight consists of collagen molecules (mostly type I, but also type III, V and VI). Keratocytes synthesize pro-a chains. Three of them form a pro-collagen triple-helix, which then self-assembles into fibrils with an uniform diameter of 22.5 to 35 nm. The highly regular organization of collagen fibrils with a homogenous inter-fibril distance (41.4 ± 0.5 nm) guarantees the high corneal transparency. Collagen fibers assemble into lamellae of about 1.5 to 2.5 μm thickness. The stroma contains about 200-300 lamellae layers going from limbus to limbus, parallel to the surface, but at various angles to one another. The space between collagen fibers is filled with glycosaminoglycans that together with core proteins form proteoglycans. Glycosaminoglycans are able to absorb large amounts of water and thus contribute to regulate the hydration state of the cornea. They provide a swelling pressure of 50 mmHg which counteracts against the pump function of the endothelium. Keratocyte cells are distributed throughout the stroma and interconnected with each other. They take the role of general repair.

DESCEMET MEMBRANE The Descemet' s membrane, increases its thickness from birth (3 μm) to adulthood (8-10 μm). It consists of collagen type IV, laminin and fibronectin. Collagen type IV fibrils are about 5-20 μm thick and weaker than type I fibrils. The main purpose of the Descemet membrane is to hinder the aqueous humor from diffusing into the stroma. After rupture it does not regenerate. When stromal swelling occurs the Descemet membrane gets folded.

ENDOTHELIUM The endothelium is the last cellular mono-layer of the cornea and forms the border to the aqueous humor. Its cells are polygonal (with a diameter of 20 μm and a thickness of 5 μm). The endothelium is the most important component of the cornea to regulate its hydration. There exists an osmotic gradient between the stroma (134 mEq/l) and the aqueous humor (143 mEqu/l), which results in a flux of sodium (Na^+) from the aqueous humor and a flux of potassium (K^+) from the stroma. Endothelial cells express Na^+- and K^+-dependent ATPase and Na^+ - K^+ exchanger. Then, in combination with carbon dioxide bicarbonate ions (HCO_3^-) are expressed and get pumped into the aqueous humor. Coupled to this HCO_3^- movement is a flux of water out of the stroma. This transport mechanism depends on cellular activity and therefore declines with cooling, which results in increasing thickness and transparency loss. Up to a certain temperature thickness and clarity are reversible. Endothelial cell density decreases with age (from average 3000-4000 cells/mm^2 in newborns to average 2000 cells/mm^2 at old age), whereby the cell diameter increases from 18-20 μm to 40 μm (polymegathism).

1.5 General Corneal Abnormalities

There are several disease that may affect the eye and then the quality of vision. the most common ones are refractive errors that lead to myopia or astigmatism, as an example.But there are also other diseases, as keratoconus, that affect an important part of population.

1.5.1 Refractive Errors

Normal vision, which has a normal refractive condition, is called emmetropia. In this condition, parallel rays of light are brought to a focus on the retina when the lens is in a relaxed accommodative state and visual acuity is 6/6 (at 6 meters) or better. In addition, near vision (at

40cm) is normal and the lens can accommodate to provide good vision. In contrast, if there is any abnormality in the refractive condition, the term ametropia describes this situation (1.7).

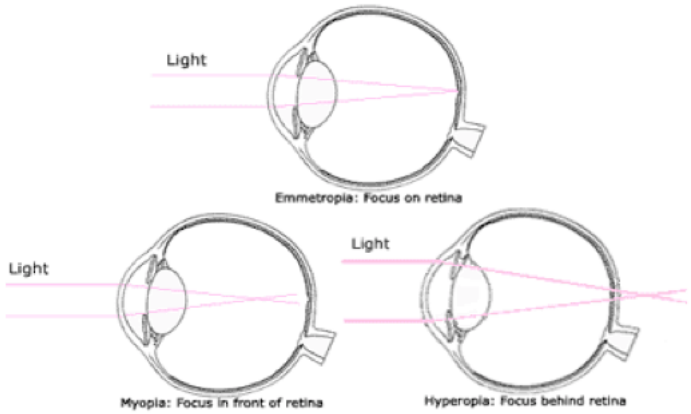

Figure 1.7: Normal and abnormal vision (refractive errors).

In this condition, parallel rays of light are not focussed onto the retina when the lens is in a relaxed accommodative state, therefore vision becomes unclear. Ametropia can be divided into three main categories which are myopia, hyperopia and astigmatism. Myopia is the situation where rays of light are focused in front of the retina and are corrected by a minus lens. Hyperopia is the situation where rays of light are focused behind the retina and are corrected by a plus lens. Astigmatism is a difference in the degree of refraction in different meridians where rays of light are dispersed and there is no specific point for the light to be focused at, and this is corrected by a cylindrical lens.

1.5.2 Keratoconus

The term *keratoconus* can be divided in two parts, *kerato* meaning cornea and *conus* meaning conical or cone-shaped, together they mean cornea with a conical shape. Keratoconus is a degenerative corneal condition which is characterized by a thinning of the corneal stroma [20] and an increase in its curvature to a more conical shape than normal [21] (fig. 1.8a). It is estimated to affect around 50 to 230 people per 100,000 [22]. Though there are increasing reports on a higher incidence of keratoconus across the world. Corneal thinning leads to myopia, irregular astigmatism and protrusion which reduce and affect the quality of vision 1.8b [21]. One of the most important points about keratoconus patients is that they never become

totally blind from this disease [23]. Usually, it is a progressive disorder, affecting both eyes, with perhaps only one eye initially affected [23], [24].

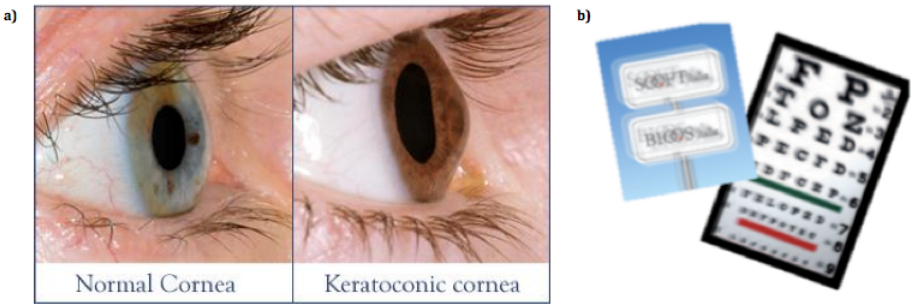

Figure 1.8: a) Normal (left) and Keratoconic (right) cornea. b) Image distortion due to keratoconus.

In 1998, Rabinowitz found some classical histopathological features in keratoconus, i.e. thinning of the corneal stroma, breaks in Bowman's layer, and deposition of iron in the basal layers of the corneal epithelium. There are a number of features noted by Krachmer et al. (1984) in keratoconus, such as the arrangement of fibrils being unregulated in the anterior stroma, in addition to a decrease in the number of collagen lamellae. In 2006, Ucakhan observed that there are some changes in the structure and composition of features of the central part of the keratoconic cornea in all layers. Until now, the causes of keratoconus have been unknown, however genetic one environmental factors play both an important role in the pathophysiology of the disease.

The authors also suggest that overexposure to ultraviolet rays from the sun, excessive eye rubbing and chronic eye irritation may lead to keratoconus.

1.5.3 Treatment

There are various and miscellaneous methods for keratoconus treatment, it all depends on the disease stage. Treatment in the very early stages of keratoconus is possible with *spectacles* and this may give patients good and adequate vision. However, spectacles are generally considered to be a temporary solution for this disease; therefore, *contact lenses* are the best option and the mainstream optical treatment for keratoconus.

In the very advanced stages of keratoconus when contact lenses become useless, *corneal transplant* (penetrating keratoplasty) is the best option for keratoconus patients [20]. *In-*

trastromal Corneal Ring implants are another refractive surgical treatment for keratoconus patients. Using surgical procedures are placed two plastic inserts in the cornea to reduce the curvature of the keratoconic corneal tissue and make this tissue flatter [28]. Currently, the most used treatment to halt or slow down the progression of keratoconus is *Corneal Cross-linking* (CXL) with Riboflavin and UVA treatment. Cross-linking is a common method of tissue stabilization. Corneal CXL is performed with ultraviolet-A (UVA) irradiation and the photosensitizer riboflavin. Riboflavin is a vitamin (vitamin B2), a yellow-orange solid substance with poor solubility in water, which chemical formula is shown in figure 1.9.

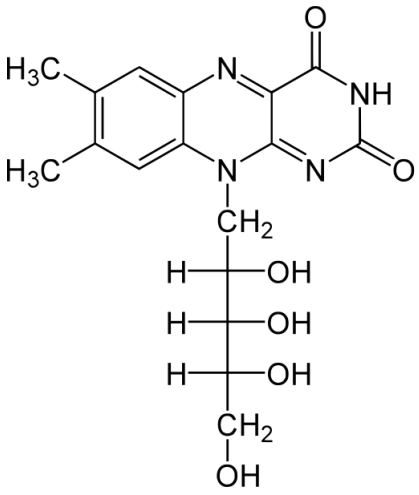

Figure 1.9: Riboflavin molecule.

1.6 Corneal Cross Linking

Photochemical CXL with Riboflavin/UVA was developed at the University of Dresden by Spoerl and Seiler. They postulated that the procedure induces physical cross-linking of collagen by Riboflavin absorbing UVA to act as a photo sensitizer to produce free radicals (oxygen singlets) that activate the natural lysyl oxidase pathway. By absorbing UVA, the Riboflavin also prevents damage to deeper ocular structures, including as the endothelium, lens and retina. The oxygen singlets are, however, thought not to instigate cross-linking by lysyl oxidase but possibly by three other mechanisms: imidazolone production, which can attach to molecules, such as histidine, to form new covalent bonds; the triggering of endogenous populations of

carbonyl groups in the ECM (allysine, hydroxyallysine) to form cross-links there, and/or the degradation of the Riboflavin molecule itself, releasing 2,3-butanedione, which can react with the endogenous carbonyl groups of the stromal proteins. The precise location of the cross-links at a molecular level is as yet undetermined. Certainly, cross-links cannot form between the collagen fibrils as the distance is too far for the formation of intra-molecular bonds. Hayes et al. in a series of ex vivo ungulate and rabbit eyes investigated corneal stromal ultrastructure using X-ray scattering, hydrodynamic behaviour and enzyme digestion and determined that it was likely that the cross links formed during Riboflavin/UVA therapy were occurring predominantly at the collagen fibril surface, rather than within the fibrils themselves, and in the protein network surrounding the collagen [29](Fig.1.10). There is no definite evidence for CXL

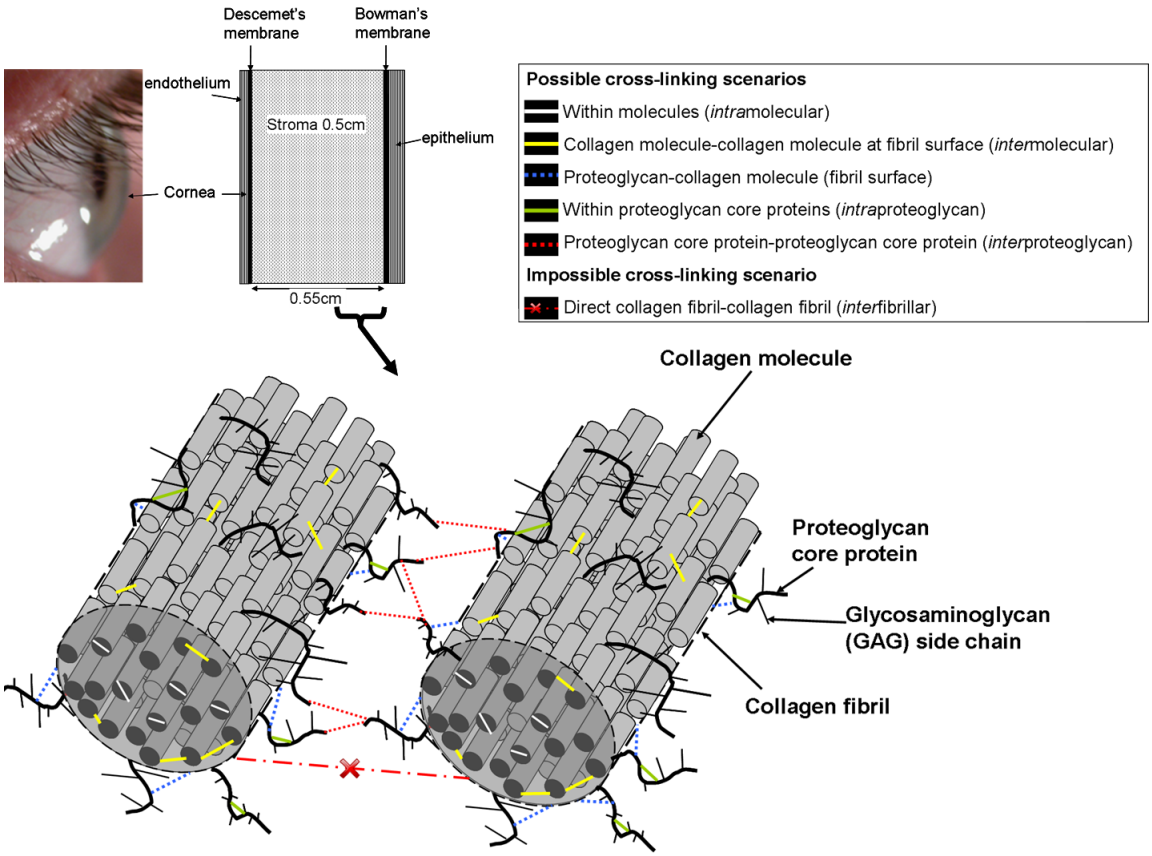

Figure 1.10: Possible cross-linking scenarios in riboflavib/UVA treatment. [30]

producing corneal collagen and protoeglycan cross-links, as these molecular bonds cannot be

seen microscopically. Ex vivo, laboratory studies, however, have reported changes in physicochemical properties of the stroma following CXL. Stress-strain measurements of corneal stromal tissue are significantly increased, both immediately as well as several months following the procedure. Immediately after irradiation an increase of the biomechanical rigidity of the cornea of about 300% is reported. These changes have been shown to principally occur in the anterior 200 μm of the stroma where the most of the UVA absorption takes place. Increased resistance of stromal tissue to enzymatic digestion has been confirmed after CXL, with a dose response in relation to the UVA intensity.

1.7 Corneal Cross-Linking Therapeutic Protocol

All patients who are candidates for CXL treatment need to have maximum keratometric readings less than 60 diopters and a central corneal thickness of at least 400 μm. The CXL procedure is conducted under sterile conditions in the operating room, after the patient's eye is anesthetized. According to the Dresden therapeutic protocol, the central 8 mm of the corneal epithelium is removed to allow better diffusion of 20% dextran riboflavin into the stroma. Because of the riboflavin's molecular weight (376g/mol) an intact epithelium would be theoretically a diffusion barrier. Therefore only after removal of the epithelium, the 20 % dextran riboflavin can penetrate the stroma. Without epithelium removal, the biomechanical effect is less than 50% of the standard cross-linking procedure. Botto's et al. [31] conclude in their 2008 study that treatment of the cornea with 20% dextran enriched riboflavin solution and UVA without previous de-epithelialization did not induce any cross-linking effect.

Following de-epithelialization, a 0.1% riboflavin solution (10 mg riboflavin-5-phosphate in 10 ml dextran 20% solution) is instilled to the cornea for 30 min (2 drops every 2 min) prior to the irradiation, until the stroma is completely penetrated and the aqueous humour is stained yellow. Changes in application time and riboflavin concentration have only little influence on stromal depth diffusion. Generally, the riboflavin film is an integral part of the CXL procedure and important in achieving the correct stromal and endothelial UVA irradiance [32]. The irradiation is performed for 30 min using a UVA double diode at 370 nm and an irradiance of 3 mW/cm^2 (equal to a dose of 5.4 J/cm^2). The required irradiance is controlled in each patient directly before the treatment to avoid a potentially dangerous UVA overdose. Instillation of riboflavin drops (1 drop every 2 min) is continued during irradiation as well, in order to sustain

the necessary concentration of riboflavin. Moreover, balanced salt solution (BSS) is applied every 6 min to moisten the cornea. A series of variations of the treatment protocol have been demonstrated. In 2009 Kanelopoulos [33] demonstrated that CXL by means of a femtosecond laser facilitated intrastromal 0.1% riboflavin administration, with promising preliminary results. In addition Bakke et al. [34] attempted to compare the severity of postoperative pain and the rate of penetration of riboflavin between eyes treated by CXL using excimer laser superficial epithelial removal and mechanical full-thickness epithelial removal, and concluded that superficial epithelial removal using the excimer laser resulted in more postoperative pain and the need for prolonged application of riboflavin to achieve corneal saturation. Contact lenses are necessary after treatment, for approximately 3 days until the epithelium heals, followed by application of fluorometholone 0.1% eyedrops for 6 weeks. In recent years researchers are also evaluating the advantages of using new riboflavin solutions that may reach the stroma avoiding the epithelium removal.

Chapter 2

CONTACT MECHANICS

Biomechanics is mechanics applied to biology. Cells are the fundamental units that support living individuals.

Biomechanics is a young interdisciplinary subject, which has only been an independent discipline for around 30-40 years [36]. In 1981, Fung [37] proposed the guidelines to study biomechanics of tissues including but not limited to the following steps: studying the geometry structure of the materials, determining the mechanical properties of the materials or tissues, understanding the environment of a functioning organ, looking for governing equations and revising with experiments, and exploring practical applications. In recent years several tissues have been investigated with different techniques to obtain informations on their mechanical properties, such as bones, cartilage, tendons etc. In this chapter, after an introduction on the main techniques used to investigate corneal biomechanics, we will briefly introduce atomic force microscopy and the force associated with this technique. We will, then, describe the most basic modulus for contact mechanics and introduce the concept of viscoelasticity. To get a better understanding of a biomechanics problem, one may need to pay attention to some properties that are generally associated with biological tissues, such as viscoelasticity, hysteresis and nonlinearity.

2.1 Corneal Biomechanics

We know from Newton's law that external force applied to an object in equilibrium will be reflected by internal forces set up within the material. If a bar is subjected to uniform tension or compression, the internal forces is referred to as direct or normal stress defined as:

$$stress(\sigma) = load/cross-section\ area \tag{2.1}$$

If such a bar is subjected to a load, it will change in length and the non dimensional deformation is referred to as strain defined as:

$$stress(\sigma) = change\ in\ length/original\ length \tag{2.2}$$

Strain is usually assumed to be the same under a given stress in compression and extension, although this assumption may be incorrect for biological materials. A materials is said to be elastic if it returns to its original unloaded dimensions when a load is removed. Hooke's law states that within certain limits of stress and strain:

$$Young's\ modulus(E) = stress/strain \tag{2.3}$$

Biological materials, such as the cornea, sclera, and extra ocular muscles, exhibit a much more complex stress/strain relationship. Infact, biologic materials show a non linear stress/strain relationship and extension of the material follows a different curve than relaxation. This phenomenon is called "hysteresis" and represents a form of viscoelastic behavior. The "viscoelastic" properties of a material may be measured in terms of creep by subjecting the material to constant force and measuring the extension over time. For an elastic material, the deformation or strain increases immediately once the load is applied and the strain maintains constant as long as the load or stress does not change. For a viscoelastic material, the deformation strain also increases once a load/stress is applied. However, the strain changes over time and eventually reaches equilibrium, even though the stress is kept at a constant level. Similarly, stress relaxation describes the phenomenon that the load or stress of the material changes when the material is subject to a specific deformation or strain. Comparing to an elastic material for which a constant strain yields a constant stress, a viscoelastic material exhibits an immediate step stress followed by a decrease of the stress until equilibrium is reached, while the material is subject to a constant strain.

The biomechanics of the cornea has been studied for many years. The majority of the current theoretical and experimental studies investigated the potential role of corneal modulus which is difficult to obtain in vivo. Several different techniques were used to estimate the stiffness of the ocular tissues, including uniaxial tensile test, inflation test, indentation, and ultrasound imaging.

The most commonly used method is the tensile test. The testing region of the tissue sample is trimmed into a rectangular shape with known width and thickness. The sample is, then, mounted on the testing device which records the relationship between force and displacement (Fig 2.1). The Young's moduli of the samples could be derived from stress-strain (force-

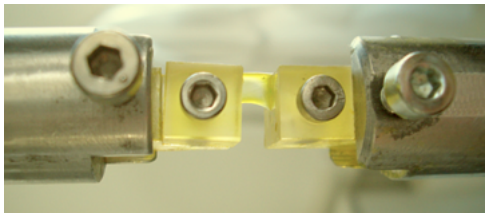

Figure 2.1: Corneal flap mounted within clamps for uni-axial stress-strain extensometer measurements.

displacement) curves. The tensile test is a straightforward way for tissue stiffness characterization with explicit stress and strain relationship, but it is also a destructive method that breaks the natural microstructure of the tissue and is based on the assumption of homogeneity in the testing sample.

The inflation test is less destructive and at least leaves the testing region intact. In the inflation test, the internal load of the ocular tissue is easily kept in simulated physiological condition. During inflating test, the apex elevation of the cornea is measured, usually with a laser beam, as a function of increasing intraocular pressure. A nonlinear pressure-displacement curve with increasing slope, typical of a nonlinear hyper-elastic material is evinced. One of the challenges in the inflation test is to accurately monitor the displacement of the sample surface, which is generally small and time dependant in ocular tissues. Also, to derive the stiffness of the sample from the inflation test results, a combined full geometric map of the sample and a mathematical model is necessary.

Owing to modern technology improvements, optical tweezers and atomic force microscopes have been used to stretch collagen molecules and fibrils in order to investigate the mechanical properties of cornea at a smaller scale (Fig. 2.2). As an example, the flexibility of collagen was tested at the molecular level by Sun et al [38] using optical tweezers. They determined

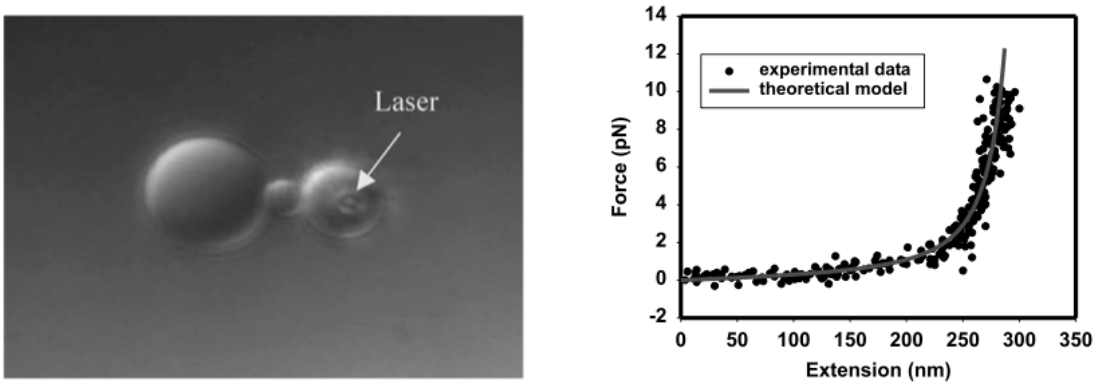

Figure 2.2: (left) Stretching of a single collagen molecule.(right) The force-extension curve for stretching a single collagen I monomer.

the mechanical properties and measured the persistence length of collagen type I monomer. The results were interpreted with the worm-like chain elasticity model which confirmed that collagen molecule is a flexible molecule.

In recent years, Atomic Force Microscopy (AFM) has been used as an investigation tool in the biological field to image the topography of soft biological materials in their native environments as well as to probe their mechanical properties. Topographical imaging involves scanning a tiny tip, attached to a flexible cantilever, across the sample surface. The interaction forces between the tip and the sample cause the cantilever to bend. A laser beam is reflected off the back of the cantilever, and small changes in cantilever deflection are detected with a position-sensitive photodiode detector. This deflection is processed by the microscope electronics to determine topological height changes on the sample surface. The achievable lateral resolution depends on the details of the tip geometry but can approach sub-nanometer levels, whereas the height resolution is of 1 Angstrom. Imaging can be accomplished in either air or fluid. In force spectroscopy mode, AFM allows to plot the deflection of the cantilever as a function of the tip distance from a specific point on the sample surface. Forces between the tip and the sample as a function of distance can be investigated. Further, information about the elasticity and viscoelasticity of materials can also be obtained. In the following we will describe the interaction forces between the tip and the sample and the models used to describe the contact mechanics between them.

2.2 Forces between Macroscopic Bodies

The integral form of interaction forces between surfaces of macroscopic bodies through a third medium (vacuum and vapor) are named surfaces forces, while those that work to hold two bodies in contact are named adhesive forces. If a process between two bodies is perfectly elastic, that is, no energy dissipates during their interaction, the adhesive and surface forces are equal in magnitude. Understanding intermolecular interactions is key to achieving control of materials at the molecular level, which is essential for various areas of physics and for nanotechnology. In soft matter van der Waals (vdW) interactions play a prominent role. The vdW forces arise from interaction between uncharged atoms or molecules, leading not only to such phenomena as the cohesion of condensed phases and physical adsorption of gases, but also to a universal force of attraction between macroscopic bodies. Friction, surface tension, viscosity, adhesion and cohesion, are also related to vdW forces. These phenomena arise from the fluctuations in the electric dipole moments of molecules which become correlated as the molecules come closer together, giving rise to an attractive force. vdW forces are the general name given to a set of forces characterized by the same power dependence on distance, having the dipole moment and the atomic polarizability as the important parameters. They include three forces of different origins, all proportional to $1/r^6$, where r is the distance between the atoms or molecules. The first contribution is due to electrostatic interactions between charges (in molecular ions), dipoles (for polar molecules), quadrupoles (all molecules with symmetry lower than cubic), and permanent multipoles. It is also referred to as Keesom force. Often, these forces occur between two molecules with permanent dipoles, i.e., they originate from the attraction between permanent dipoles and are temperature dependent. The second contribution is the induction (also known as polarization) or Debye force, arising from interactions between rotating permanent dipoles and from the polarizability of atoms and molecules (induced dipoles). These induced dipoles occur when one molecule with a permanent dipole repels another molecule's electrons. A molecule with permanent dipole can induce a dipole in a similar neighboring molecule and cause mutual attraction. The forces between induced and permanent dipoles are not as temperature dependent as Keesom interactions because the induced dipole is free to shift and rotate around the non-polar molecule. The Debye induction effects and Keesom orientation effects are referred to as polar interactions. The third and dominant contribution is the dispersion or London force (fluctuating dipole-induced dipole), due to the non-zero instantaneous dipole moments of all atoms and molecules. Such polarization

can be induced either by a polar molecule or by the repulsion of negatively charged electron clouds in non-polar molecules. Thus, London interactions are caused by random fluctuations in electron density in an electron cloud. The dispersion (London) force is the most important component because all materials are polarizable, whereas Keesom and Debye forces require permanent dipoles.

Hamaker developed the theory of vdW forces between macroscopic bodies in 1937 and showed that the additivity of these interactions makes them considerably more long-range. There are two approaches to calculating the vdW interaction between two macroscopic bodies as a function of their separation distance. The first one, referred to as the Hamaker approach, determines the vdW interaction by carrying out the so-called Hamaker-type integration of all the intermolecular interactions. The second approach, based on the Lifshitz theory, is more rigorous and gives the vdW interaction energy as a function of macroscopic electrodynamic properties of the interacting media, such as their dielectric permittivities and refractive indices. However, the vdW interaction is non-additive; i.e., the interaction of two bodies is affected by the presence of other bodies, and a simple sum of the pair-wise interactions is usually greater than the actual force between the macro bodies. The degree of non-additivity may depend on the density of the medium, i.e., for rarefied media it is possible to assume additive forces. Hamaker used the following approximations: the total interaction is obtained by the pair-wise summation of the individual contributions (additivity); the summation can be replaced by an integration over the volumes of the interacting bodies assuming that each atom occupied a specific volume, with a density (continuous medium); ρ and C that should be uniform over the volume of the bodies (homogeneous material properties). Using Hamaker's approximation, the force between two surfaces as a sphere of radius R and a flat surface may be written as

$$F(D) = -\frac{AR}{6D^2} \tag{2.4}$$

and the vdW potential as

$$W(D) = -\frac{AR}{6D} \tag{2.5}$$

A is the Hamaker's coefficient (or constant), being equal to:

$$A = \pi^2 C_L \rho_1 \rho_2 \tag{2.6}$$

The Hamaker constant depends on C_L, a microscopic property of two interacting atoms, then ultimately depends on the strength of the interaction between bodies and the medium surrounding them. A also depends on the densities of both materials and it has the dimension of an energy. In Hamaker's approximation, many-body effects of an intervening liquid medium and retardation effects for large distances an ignored. To overcome this problem, Lifshitz presented an approach taking into account multi-body interaction trough the use of the static and frequency-dependent dielectric constant, ϵ_r, and refractive index, n. Within Lifshitz's derivation, the Hamaker constant for interaction of medium 1 and 2 across medium 3 (immersion medium) is:

$$A \cong \frac{3}{4} kt \left(\frac{\epsilon_1 - \epsilon_3}{\epsilon_1 + \epsilon_3}\right)\left(\frac{\epsilon_2 - \epsilon_3}{\epsilon_2 + \epsilon_3}\right) + \frac{3h}{4\pi} \int_{\nu_1}^{\infty} \left(\frac{\epsilon_1(\nu) - \epsilon_3(\nu)}{\epsilon_1(\nu) + \epsilon_3(\nu)}\right)\left(\frac{\epsilon_2(\nu) - \epsilon_3(\nu)}{\epsilon_2(\nu) + \epsilon_3(\nu)}\right) d\nu \tag{2.7}$$

The equation above highlights the important characteristics for vdW forces:

1. the vdW force between two identical bodies in a medium is always attractive (A is positive), whereas the force between two different bodies may be attractive or repulsive. If ϵ_3 and n_3 are intermediate between ϵ_1 and ϵ_2 and n_1 and n_2, respectively, A is negative (repulsive);

2. the vdW force between any two condensed bodies in vacuum or in air ($\epsilon_3 = 1$ and $n_3 = 1$) is always attractive (A is always positive);

3. If ϵ_3 and n_3 equal the dielectric constant and index of refraction of either of the two bodies, A vanishes;

4. The vdW force is much reduced in a solvent medium.

Then, the interactions between two surfaces depend on whether the system is in vacuum, in air or ambient conditions or in a liquid. In vacuum, there are long-range vdW and electrostatic (Coulombic) forces, while at smaller surface separations corresponding to molecular contact (D ~ 0.1-0.2 nm) there are additional forces such as covalent, hydrogen and metallic bonding forces. All of these forces determine the adhesion between bodies of different geometries, the surface and interfacial energies of planar surfaces, and the strengths of materials, grain boundaries, cracks, and other adhesive junctions. When exposed to a vapor, e.g., atmospheric air, two solid surfaces in or close to contact may have a surface layer of chemisorbed or physisorbed molecules, or a capillary condensed liquid bridge between them. Each of these effects can drastically modify adhesion. The adhesion force usually decreases, but in the case of

capillary condensation, the additional Laplace pressure between the surfaces may cause the adhesion to be stronger than in an inert gas or vacuum. The force between two surfaces totally immersed in a liquid is again different from that in vacuum or air. An atomic force microscope is a powerful tool to measure vdW and adhesion forces between two macroscopic bodies.

2.3 Contact Mechanics

Analyzing the interaction of a tip with a sample surface, the mechanical properties of materials such as the local elastic modulus, and viscoelasticity can be measured. It should be noted that with the AFM, the modulus is measured in compression as the AFM tip is indented into the sample surface. The modulus measured with AFM may, therefore, be different from that obtained from other techniques, such as tensile testing, because of the differences in the direction of applied strain and any anisotropy of the sample. AFM, however, has the force sensitivity and the spatial resolution necessary to measure the local modulus of very soft sample surfaces and to investigate sample heterogeneities across small size scales. The interaction between an AFM tip and a surface may be interpreted with the general theory of contact mechanics. During nanoindentation, a tip of known mechanical properties compresses a sample of unknown mechanical properties. "Contact mechanics" is the study of the stresses and deformation that arise when two elastic solids come in contact with each other. Several contact mechanical models have been developed to characterize this interaction. These models take into account the geometry of the indenter as well as the thickness and adhesion characteristics of the sample. The models described in the following are the most common contact mechanical models that have been applied to indentation experiments.

2.3.1 Hertz Model

Heinrich Hertz, in his 1881 pioneer paper titled "On the contact of elastic solid", solved the problem of the elastic contact between two spheres that can be extended to a sphere in contact with flat surface [39]. His approach assumes that adhesion and surface forces can be neglected. He considered two spheres (radii R_1 and R_2) compressed by a force F_N resulting in a contact area of radius a and assuming only elastic deformations of the materials (Fig. 2.3). Hertz derived equations for the contact radius a and the indentation depth δ between the

spheres:

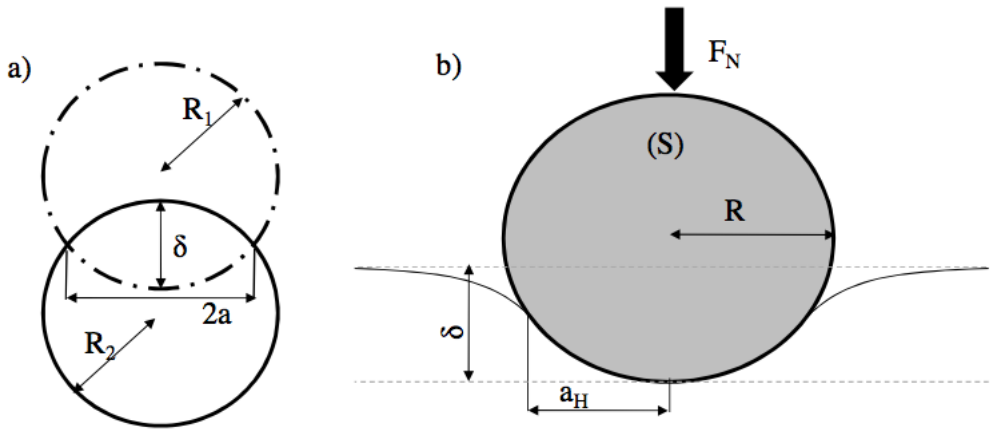

Figure 2.3: Hertz model a) for two compressed spheres (radii R_1 and R_2) and b) for an elastic sphere (S) in contact with an elastic half space.

$$a = \left(\frac{3F_N R}{4E}\right)^{1/3} \tag{2.8}$$

$$\delta = \frac{a^2}{R^*} \tag{2.9}$$

where R^* describes the effective sphere radius and E^* the effective Young's modulus defined as:

$$\frac{1}{E^*} = \frac{1-\nu_1^2}{E_1} + \frac{1-\nu_2^2}{E_2} \tag{2.10}$$

$$R^* = \frac{R_1 R_2}{R_1 + R_2} \tag{2.11}$$

Here E_i are the Young's moduli and ν_i the Poisson ratios of the two bodies. The penetration depth δ is proportional to the $F^{2/3}$

$$\delta = \sqrt[3]{\frac{9F_N^2}{16E^* R^*}} \tag{2.12}$$

And correspondingly, the force to achieve a certain penetration δ is given as:

$$F_N = \frac{4}{3} E^* \sqrt{R^*} \delta^{3/2} \tag{2.13}$$

A relation between the force and the contact radius can be observed

$$F_N = \frac{4}{3} E^* \sqrt{R^*} \left(\frac{a^2}{R^*} \right)^{3/2} \tag{2.14}$$

The proportionality between the contact radius and the area of contact lead to a proportionality of both with the force

$$a \propto F_N^{1/3} \tag{2.15}$$

$$A_R = \pi a^2 \tag{2.16}$$

Moreover, the total force compressing the solids can be expressed in relation to the pressure by:

$$F_N = \int_{-a}^{a} P(r) 2\pi r dr \tag{2.17}$$

where *P(r)* is the pressure distribution over the contact and is given by Hertz to be

$$P(r) = P_0 \sqrt{\left(1 - \left(\frac{r}{a}\right)^2\right)} \tag{2.18}$$

where *r* ranges from *-a* to *a*. Eq. 2.18 shows that the contact pressure is zero at the edges and is maximum at the center of the contact. Therefore the maximum pressure of contact would be

$$P_0 = \frac{3F_N}{2\pi a^2} = \frac{3}{2\pi} \sqrt[3]{\frac{16 F_N E^{*2}}{9 R^{*2}}} \tag{2.19}$$

The average pressure can be given by the force acting on the area of contact:

$$P_m = \frac{F_N}{\pi a^2} = \frac{1}{\pi} \sqrt[3]{\frac{16 F_N E^{*2}}{9 R^{*2}}} \tag{2.20}$$

The Hertz theory allows calculating the contact shape and forces between two contacting surfaces under the influence of an external force. It does not include any surface force and therefore the Hertz model describes accurately the contact between elastic bodies in the absence of adhesion The fact that the adhesion is not considered in this model leads to big errors in calculations where attractive forces play the dominant role. In 1971 Johnson, Kendall and Roberts (JKR) extended the Hertz model to include adhesion effects.

2.3.2 Sneddon Model

In 1948 and further on in 1965, Sneddon proposed that the elastic load-displacement relationships for many simple indenter geometries can conveniently be written as

$$F = \alpha \delta^m \tag{2.21}$$

where F is the indenter load, δ is the elastic displacement of the indenter, and α and m are constants. Values of the exponent m for different indenter geometries can be reported namely $m = 1$ for flat cylinders, $m = 1.5$ for spheres and paraboloids of revolution, $m = 2$ for cones in the limit of small displacement (i.e. linear deformation). For small displacements, a conventional method for extracting the elastic properties from indentation data relies on the solution derived by Sneddon that complete the Hertzian formulation valid for spheres to any shape of revolution solids in contact with a plane. Sneddon showed that the load-displacement relationship for different geometries can be written as

$$F = C_T E_r \delta^m \tag{2.22}$$

where F is the indenter load, C_T contains the indenter geometry constants, E_r refers to the reduced modulus containing the material properties.

2.4 The Johnson-Kendall-Roberts Model

Adhesion plays an important role on the length scales we are interested in and hence it should be taken into account when small objects in contact are used. An extension of the Hertz theory taking into account surface forces was elaborated in 1971 by Johnson, Kendall and Roberts [26] and it has become well known as the JKR theory. Their basic assumption was to take into account the adhesive interaction only within the contact zone and neglect any interaction outside the contact zone (Fig. 2.4). JKR model considers that γ is the work per unit of area necessary to separate the tip and the surface of study. γ can be written as follows:

$$\gamma = \gamma_1 + \gamma_2 - \gamma_{1,2} \tag{2.23}$$

Where, γ_1 and γ_2 stand for the surface energies of the two contacting bodies and $\gamma_{1,2}$ is the interfacial energy. As γ value takes into account all the different attractive forces arising between

the tip and the sample, this model is particularly suitable for tips with a large R value and for sticky surfaces, as these two factors will result in a noticeable increment of attractive van der Walls forces. Nevertheless, this model considers that the attractive forces only take place when the two surfaces are in contact and no effect is noticed by the tip as it approaches the sample. Then, *JKR model* assumes that all interaction forces have zero range. In order words, the surfaces only gain energy if they touch, but not if they are separated by an infinitesimal amount or more. Due to that, JKR model refines Hertz considerations but still fail to model surface interactions before the contact [40].

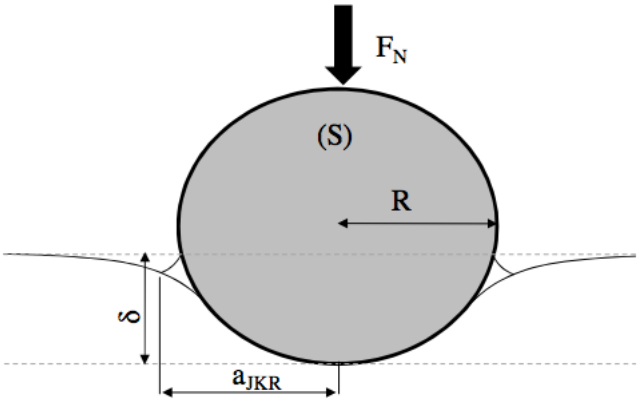

Figure 2.4: The JKR model for a rigid sphere (S) in contact with an elastic half space.

The JKR contact radius a_{JKR} and the JKR indentation depth δ are given as a function of the externally applied load F for an elastic sphere in contact with elastic half space as,

$$a_{JKR} = \left(\frac{3R}{4Y^*}\left[F + 3\pi R\gamma + \sqrt{6\pi R\gamma F + (3\pi R\gamma)^2}\right]\right)^{1/3} \tag{2.24}$$

$$\delta = \frac{a^2}{R} - \sqrt{\frac{2\pi a\gamma}{Y^*}} \tag{2.25}$$

where γ is the effective surface energy of adhesion of both surfaces. In this case, they found a larger contact area compared to the contact area in the Hertz model,

$$A_R = \pi a^2 = \left(\frac{3\pi R}{4Y^*}\left[F + 3\pi R\gamma\sqrt{6\pi R\gamma F + (3\pi R\gamma)^2}\right]\right)^{2/3} \tag{2.26}$$

By assuming the friction force is proportional to the real area of contact the previous equation will lead to a sub linear dependence of the friction force on the load. Furthermore, in the

absence of surface forces ($\gamma = 0$) equations 2.16 and 2.17 reduce to the classical Hertz model. However, the JKR approach of the contact of two elastic bodies is not right in every case, since it neglects the forces acting at the border of the contact area.

2.5 The Derjaguin-Muller-Toporov Model

The alternative thermodynamic approach by Derjaguin, Muller and Toporov (DMT, 1975) [41], assumes that the contact area does not change due to the attractive surface forces and remains the same as in the Hertz theory. In this model the attractive forces are assumed to act only outside of the contact area. Due to the involved assumptions, the JKR model is more suitable for compliant materials and the DMT model is more appropriate for rigid materials. In the DMT model the attractive force is simply added as an additional load to obtain the correct indentation depth and contact area from the Hertz theory. Therefore the equations for the contact radius and the indentation depth in the case of a sphere indenting a plane become

$$a_{DMT} = \left(\left(\frac{3\pi R}{4E^*}\right)(F + 4\pi\gamma R)\right)^{1/3} \tag{2.27}$$

$$\delta = \frac{a^2}{R} \tag{2.28}$$

In the case of DMT, they obtained an area of contact given by

$$A_R = \pi a^2 = \left(\left(\frac{3\pi R}{4E^*}\right)(F + 4\pi\gamma R)\right)^{2/3} \tag{2.29}$$

The DMT model takes into account the surface forces outside the contact area but not the deformations due to these forces. Therefore, one might expect that the JKR model is more appropriate for the case of compliance contacts and high surface energies, whereas the DMT model should be better suited for the case of rigid contacts and low surface energies.

2.6 Viscoelasticity

The material response discussed in the previous section was limited to the response of elastic materials. For an elastic material, the normal stress σ is a function of normal strain ϵ only. For

a linearly elastic material, stress is linearly proportional to strain, and in the case of normal stress and strain, the constant of proportionality is the elastic modulus E of the material

$$\sigma = E\epsilon \tag{2.30}$$

While investigating the response of an elastic material, the concept of time does not enter into the discussions. Elastic materials show time-independent material behavior. Elastic materials deform instantaneously when they are subjected to externally applied loads. They resume their original (unstressed) shapes almost instantly when the applied loads are removed. There is a different group of materials such as polymer plastics, almost all biological materials, and metals at high temperatures that exhibits gradual deformation and recovery when they are subjected to loading and unloading. The response of such materials is dependent upon how quickly the load is applied or removed, the extent of deformation being dependent upon the rate at which the deformation-causing loads are applied. This time-dependent material behavior is called viscoelasticity. Viscoelasticity is made up of two words: viscosity and elasticity. Viscosity is a fluid property and is a measure of resistance to flow. Elasticity, on the other hand, is a solid material property. Therefore, a viscoelastic material is one that possesses both fluid and solid properties. For viscoelastic materials, the relationship between stress and strain can be expressed as:

$$\sigma = \sigma(\epsilon, \dot{\epsilon}) \tag{2.31}$$

Eq. 2.31 states that stress, σ, is not only a function of strain, ϵ, but is also a function of the strain rate, $\dot{\epsilon}=d\epsilon/dt$, where t is time. Eq. 2.31 indicates that the stress-strain diagram of a viscoelastic material is not unique but is dependent upon the rate at which the strain is developed in the material. An elastic material deforms, stores potential energy, and recovers deformations in a manner similar to that of a spring. The elastic modulus E for a linearly elastic material relates stresses and strains, whereas the constant k for a linear spring relates applied forces and corresponding deformations (fig. 2.5). Both E and k are measures of stiffness. The similarities between elastic materials and springs suggest that springs can be used to represent elastic material behavior. Since these similarities were first noted by Robert Hooke, elastic materials are also known as Hookean solids.

When subjected to external loads, fluids deform as well. Fluids deform continuously, or flow. For fluids, stresses are not dependent upon the strains but on the strain rates. If the stresses and strain rates in a fluid are linearly proportional, then the fluid is called a linearly

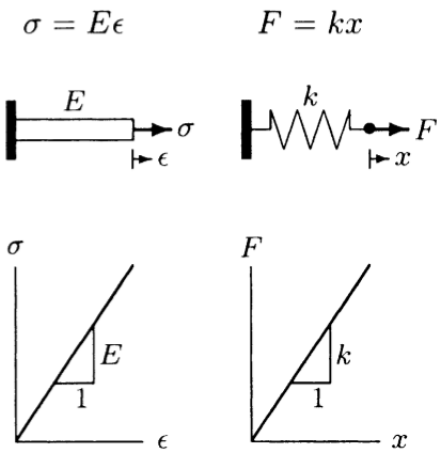

Figure 2.5: Analogy between a linear spring and an elastic solid

viscous fluid or a Newtonian fluid. Examples of linearly viscous fluids include water and blood plasma. For a linearly viscous fluid,

$$\sigma = \eta(\dot{\epsilon}) \tag{2.32}$$

In Eq. 2.32, η is the constant of proportionality between the stress σ and the strain rate $\dot{\epsilon}$, and is called the coefficient of viscosity of the fluid. As illustrated in Fig. 2.6, the coefficient of viscosity is the slope of the graph of a Newtonian fluid. The physical significance of this coefficient is similar to that of the coefficient of friction between the contact surfaces of solid bodies. The higher the coefficient of viscosity, the "thicker" the fluid and the more difficult it is to deform.

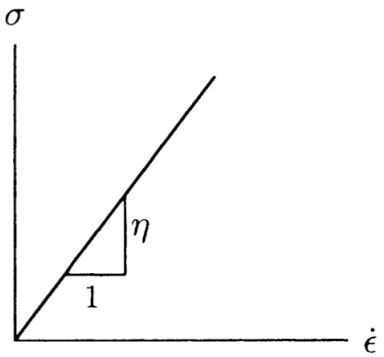

Figure 2.6: Stress-strain rate diagram for a linearly viscous fluid.

The spring is one of the two basic mechanical elements used to simulate the mechanical behavior of materials. The second basic mechanical element is called the dashpot, which is used to simulate fluid behavior. As illustrated in Fig. 2.7, a dashpot is a simple piston-cylinder or a syringe type of arrangement. A force applied on the piston will advance the piston in the direction of the applied force. The speed of the piston is dependent upon the magnitude of the applied force and the friction occurring between the contact surfaces of the piston and cylinder. For a linear dashpot, the applied force and speed (rate of displacement) are linearly proportional, the coefficient of friction μ being the constant of proportionality. If the applied force and the displacement are both in the x direction, then,

$$F = \mu \dot{x} \tag{2.33}$$

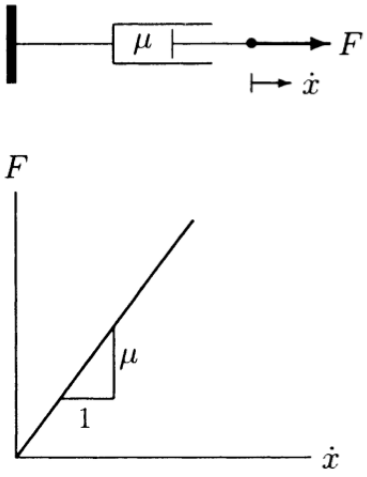

Figure 2.7: A linear dashpot and its force-displasement rate diagram.

In Eq. 2.33, $\dot{x}$=dx/dt is the time rate of change of displacement or the speed. By comparing Eqs. 2.32 and 2.33, an analogy can be made between linearly viscous fluids and linear dashpots. The stress and the strain rate for a linearly viscous fluid are, respectively, analogous to the force and the displacement rate for a dashpot; and the coefficient of viscosity is analogous to the coefficient of viscous friction for a dashpot. These analogies suggest that dashpots can be used to represent fluid behavior.

Springs and dashpots constitute the building blocks of model analyses in viscoelasticity. Springs and dashpots connected to one another in various forms are used to construct empirical viscoelastic models. Springs are used to account for the elastic solid behavior and dashpots

are used to describe the viscous fluid behavior. It is assumed that a constantly applied force (stress) produces a constant deformation (strain) in a spring and a constant rate of deformation (strain rate) in a dashpot. The deformation in a spring is completely recoverable upon release of applied forces, whereas the deformation that the dashpot undergoes is permanent.

The simplest forms of empirical models are obtained by connecting a spring and a dashpot together in parallel and in series configurations. As illustrated in Fig. 2.8, the Kelvin-Voight model is a system consisting of a spring and a dashpot connected in a parallel arrangement. As shown in Fig.2.9, the Maxwell model is constructed by connecting a spring and a dashpot

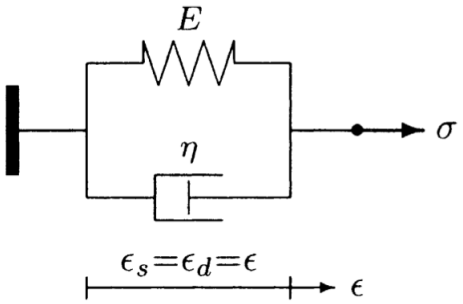

Figure 2.8: Kelvin-Voight model.

in a series. In this case, a stress σ applied to the entire system is applied equally on the spring and the dashpot ($\sigma = \sigma_s = \sigma_d$), and the resulting strain ϵ is the sum of the strains in the spring and the dashpot ($\epsilon = \epsilon_s = \epsilon_\delta$).

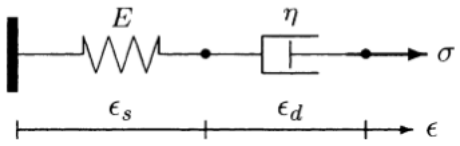

Figure 2.9: Maxwell model.

The Kelvin-Voight solid and Maxwell fluid are the basic viscoelastic models constructed by connecting a spring and a dashpot together. They do not represent any known real material. However, in addition to springs and dashpots, they can be used to construct more complex viscoelastic models, such as the standard solid model. As illustrated in Fig. 2.10, the standard solid model is composed of a spring and a Kelvin-Voight solid connected in a series. The standard solid model is a three-parameter (E_1, E_2, and η) model and is used to describe the

viscoelastic behavior of a number of biological materials such as the cartilage and the white blood cell membrane.

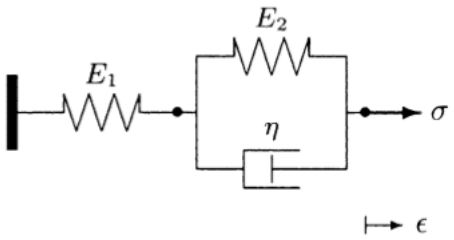

Figure 2.10: Standard solid model.

2.7 Comparison of Elasticity and Viscoelasticity

There are various criteria with which the elastic and visco-elastic behavior of materials can be compared. As mentioned before, viscoelastic materials exhibit time-dependent material behavior. The response of a viscoelastic material to an applied stress not only depends upon the magnitude of the stress but also on how fast the stress is applied to or removed from the material. Consequently, as illustrated in Fig.2.11, a viscoelastic material does not have a unique stress-strain diagram. For an elastic body, the energy supplied to deform the body (strain en-

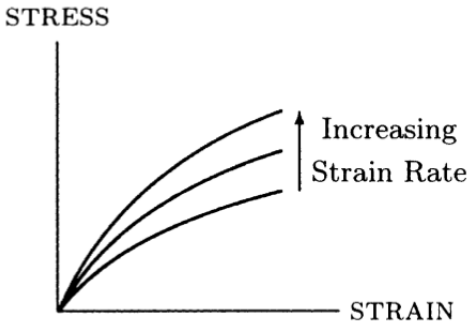

Figure 2.11: Stress-strain diagram for a viscoelastic material may not be unique.

ergy) is stored in the body as potential energy. This energy is available to return the body to its original (unstressed) size and shape once the applied stress is removed. As illustrated in

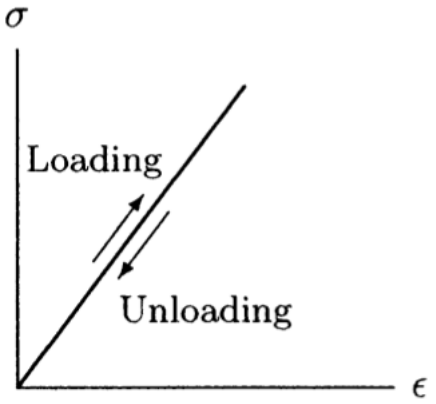

Figure 2.12: For an elastic material, loading and unloading paths coincide.

Fig.2.12, the loading and unloading paths for an elastic material coincide. This indicates that there is no loss of energy during loading and unloading.

For a viscoelastic body, some of the strain energy is stored in the body as potential energy and some of it is dissipated as heat. For example, consider the Maxwell model. The energy provided to stretch the spring is stored in the spring while the energy supplied to deform the dashpot is dissipated as heat due to the friction between the moving parts of the dashpot. Once the applied load is removed, the potential energy stored in the spring is available to recover the deformation of the spring, but there is no energy available in the dashpot to regain its original configuration. Consider the three-parameters standard solid model shown in Fig.2.10 typical loading and unloading diagram for this model is shown in Fig.2.13. The area enclosed by the loading and unloading paths is called the hysteresis loop, which represents the energy dissipated as heat during the deformation and recovery phases. This area, and consequently the amount of energy dissipated as heat, is dependent upon the rate of strain employed to deform the body. The presence of the hysteresis loop in the stress-strain diagram for a viscoelastic material indicates that continuous loading and unloading would result in an increase in the temperature of the material. Viscoelastic materials dissipate energy regardless of whether the strains or stresses are small or large. Since viscoelastic materials exhibit time-dependent material behavior, the differences between elastic and viscoelastic material responses are most evident under time-dependent loading conditions.

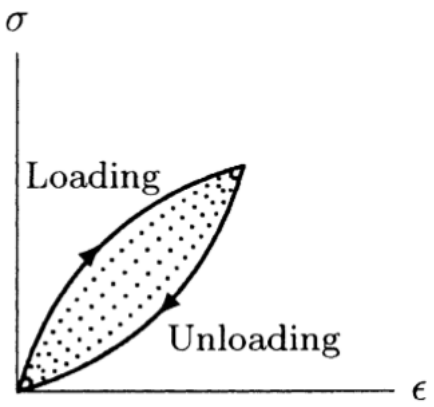

Figure 2.13: Hysteresis loop.

Chapter 3

ATOMIC FORCE MICROSCOPY

The Atomic Force Microscope was invented in 1986 by Gerd Binnig, Calvin F. Quate and Chistopher Gerber [42]. The most significant advantage of the atomic force microscopy technique is that samples may be examined with minimal preparation and, hence, with low risk of altering the surface features. Furthermore, atomic force microscopy provides extraordinary topographic contrast, clear views of the surface features and the possibility of imaging in a natural environment (air or liquid). In the last decade, AFM has become one of the most used imaging technique in the biological field and it is being extensively used in the field of ophthalmology.

In the following section we will describe the main parts of an AFM and its basic operating principles.

3.1 Working Principle

An AFM consists essentially of a tip attached to a flexible lever, a piezoelectric scanner that moves the sample under the tip, an optical detection system that detects the cantilever movement and a feedback loop. A motorized system is used to quickly bring the tip in proximity of the surface. Once the tip starts interacting with the surface, the motor stops and the tip-sample distance is controlled by the piezoelectric scanner. The scanner is able to extend and contract with sub-nm steps at distances ranging from nm to tens of microns in the plane parallel to the sample and from nm to few microns in the direction perpendicular to the sample. Once the tip and the sample are in contact, the scanner starts to move the sample under the tip. As

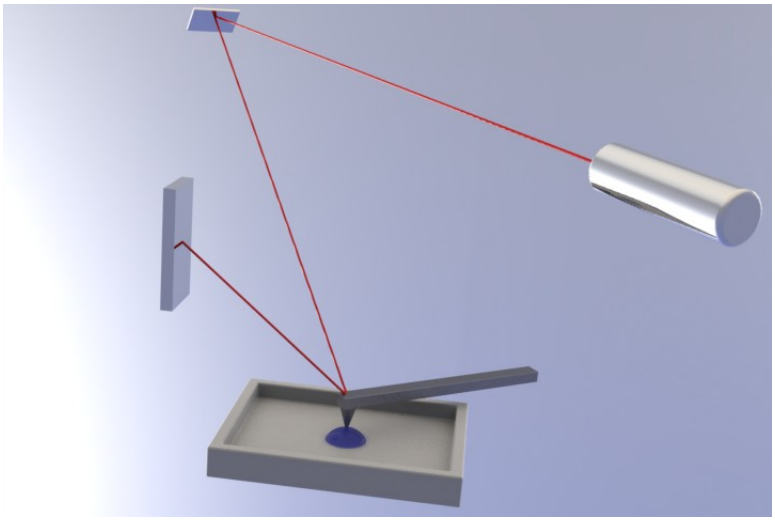

Figure 3.1: Schematic representation of an optical detection system based on the reflection of a laser beam.

mentioned above, the deflection of the lever is controlled by an optical detection system. This system, also known as optical lever, is composed of a small laser diode and a four-segments photodiode. When the lever bends up and down, so the laser spot does on the photodiode. The optical lever magnifies the nanoscale deflection of the lever and makes it detectable by the photodiode. While the tip moves on the sample surface, these movements are recorded together with the lever deflection and are used to build a three dimensional image of the surface.

3.2 Scanner and Optical Lever

During the image acquisition, the scanner movements X, Y are controlled by the computer that generates two synchronized voltage ramps, allowing for the scanning of the chosen sample area, whereas the movement of the Z piezo is controlled by the feedback circuit, that keeps constant the lever deflection (fig. 3.2).

Fig.3.3 shows the raster pattern of the scanner. The scanner moves the sample along the fast scan direction by steps of length L/N, where L is the linear dimension of the scanned area and N is the total number of points that are acquired for each line [43]. At each step the specimen z-height is sampled and in this way the first array of heights is acquired. At the end of the first line, the controller will move the piezo stage one step in the slow scan direction and the

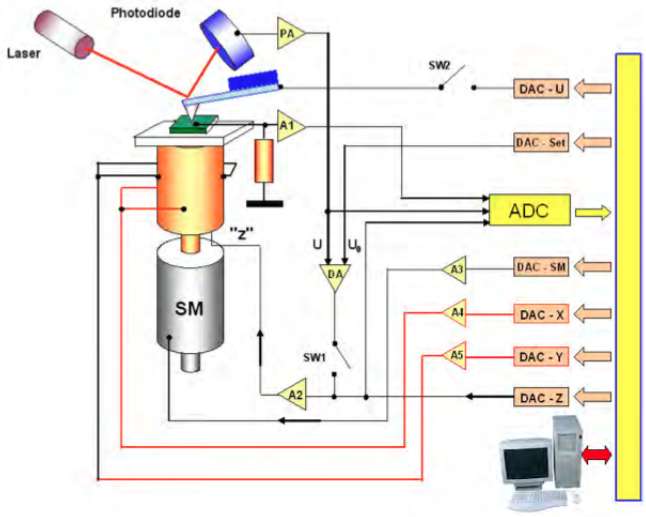

Figure 3.2: AFM scheme.

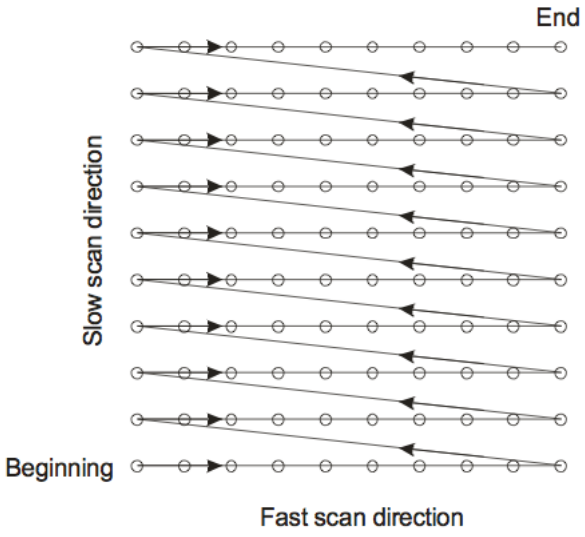

Figure 3.3: Scanning raster pattern.

acquisition restarts. This process will be iterated N times, in order to acquire a N x N matrix in which each element corresponds to a point on the sampled area, and its value is the height of that point. Nevertheless, most AFM microscopes allow to acquire both the trace and the retrace pathways before the next step in the slow scan direction.

3.3 AFM Tips

Typical AFM tips are grown on cantilevers by micro fabrication methods [44] from Si or Si_3N_4. The tip has micro metric dimensions and it can also have different geometries as conical, pyramidal or spherical. The main factor affecting lateral resolution in an AFM image is the radius of curvature of the tip apex, which can vary from few nanometers to tens of microns. For our experiments we have used both conical and spherical tips. Conical tips are commercially available (fig. 3.4a)while spherical tips were obtained by modifying standard AFM tips with glass microspheres, thereby increasing the surface contact area to measure the mechanical response of the tissue rather than that of the individual tissue components (Last et al., 2009). Tipless AFM cantilevers (nominal spring constant: 4.5 N/m, NSC12 series, Mikromasch, San Jose, CA) were modified with glass microspheres (59-74 μm diameter, 15926-100, Polysciences Inc.) by using a water-resistant two-part epoxy adhesive to attach a microsphere onto the cantilever with the aid of an inverted optical microscope (Carl Zeiss Stemi-2000C), allowing it to dry overnight, and then rinsing it in ethanol to remove excess epoxy from the tip [47] (fig. 3.4b). The AFM systems used in these studies are a nano scope IIIa Commercial AFM (BRUKER) and a custom laboratory built AFM design used for imaging [45], [46].

3.4 Cantilever Elastic Constant

A key parameter in our study is the calibration of the cantilevers' elastic constant. In the last years several methods for determining cantilever beam stiffness have been presented, each with advantages and limitations [48]. Cleveland's method involves measurement of the resonance of the beam before and after loading it with a known mass [49]. Although highly accurate, this method is tedious and time-consuming and can lead to damage of the cantilever tip. A second method involves measuring the thermal resonance spectrum of the cantilever and fitting a simple harmonic oscillator model to it [50]. A third method involves the measurement

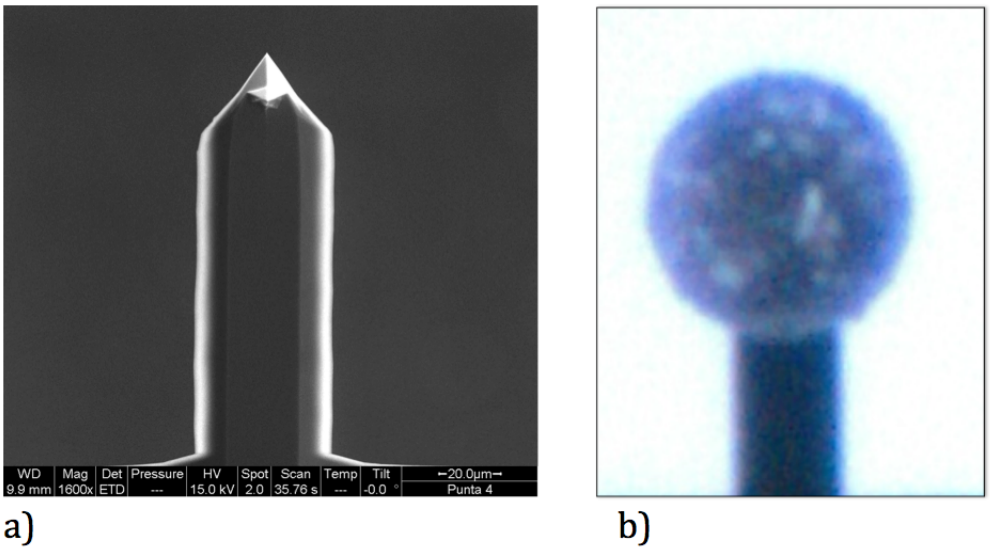

Figure 3.4: a. SEM image, top view of the entire cantilever beam; b.AFM tip modified with a microsphere.

of the dimensions of the lever and the calculation of its stiffness by assuming a known density and Young's modulus. The simplicity of this method serves as the basis for its widespread popularity. We have used this method to determine the elastic constant of commercially available cantilevers (TAP 300 BRUKER) with conical tips. These cantilevers have a trapezoidal section and an almost rectangular shape. From Euler-Bernoulli beam theory, the stiffness, k, of rectangular beams is proportional to I, the second moment of its cross sectional area

$$k = 3EI \,/\, l^3 \tag{3.1}$$

where l is the beam length and E is its Young's modulus. Geometrically, the second moment of a beam with a trapezoidal cross section, $I_{trapezoid}$, is

$$I_{trapezoid} = \frac{t^3(a^2+4ab+b^2)}{36(a+b)} \tag{3.2}$$

where t is the beam thickness, a is the width of the top face (tip side) of the beam, and b is the width of the bottom face.

For the calibration of colloidal probe cantilevers we have used another approach. Gibson et al., as well as Tortonese and Kirk, have developed a "beam on beam" approach, where the cantilever is brought into contact with a calibrated standard cantilever beam [51] [52]. The accuracy of this straightforward method is limited by the certainty to which the reference beam

stiffness is known, the positioning of the tip onto the end of the reference beam, and the calibration of the photodiode sensitivity and scanner vertical movement. This method is more appropriate since the bead mass is bigger than the one of a conical tip. For the calibration we have exploited the known spring constant of Force Calibration Cantilevers (model CLFC), pre-calibrated by Bruker . The procedure is done through the following simple steps:

- Selection of the appropriate CLFC cantilever by comparing the nominal spring constant of the unknown cantilever, k_{nom}, to the known spring constants of CLFC cantilevers (k_{ref}). For the best accuracy, a CLFC cantilever must be selected with spring constant such that $0.3\ k_{ref} < k_{nom} < 3\ k_{ref}$;

- After mounting the probe on a sample disc using double-sided tape, the CLFC cantilever is positioned on the AFM sample stage, such that its long axis is aligned with the cantilever to be calibrated, but facing the opposite direction, as shown (in fig.3.5.a).

- After aligning the cantilever to be calibrated over the substrate of the CLFC probe, as shown in fig.3.5b, and engaging normally in contact mode, the deflection sensitivity is measured in ramp mode;

- After, the cantilever to be calibrated is withdrawn and realigned close to the end of the CLFC cantilever as shown in fig.3.5.c. Several measurements of the deflection sensitivity and an average of the results is done to obtain the average deflection sensitivity on the CLFC cantilever, S_{ref};

- Then, the offset $\triangle$ L of the tip from the end of the reference cantilever is measured;

- The spring constant of the unknown cantilever is calculated using the following formula:

$$k = k_{ref}\Big(\frac{S_{ref}}{S_{hard}-1}\Big)\Big(\frac{L}{L-\triangle L}\Big)^3 \tag{3.3}$$

  Uncertainty in the calibration is dominated by error in determining the deflection sensitivity values [53].

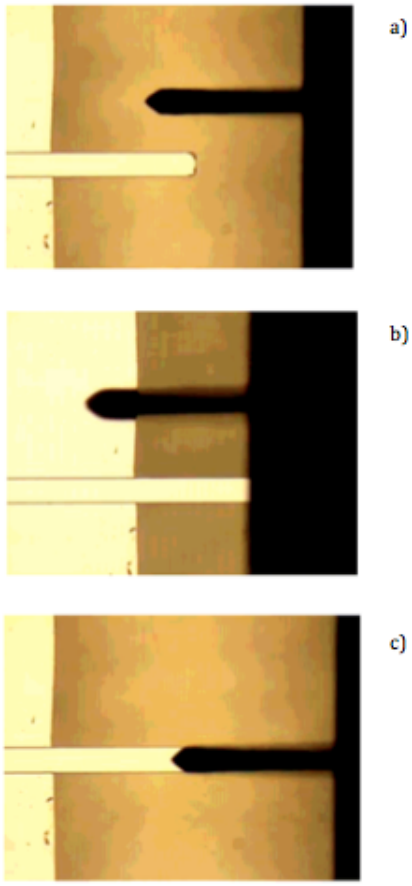

Figure 3.5: Calibration using a CLFC.

3.5 AFM Operating Modes

An AFM can be used to acquire the topography of a sample surface as well as to measure its mechanical properties. In the following section we will briefly introduce the imaging and the force spectroscopy mode.

3.5.1 Imaging modes

To image sample topography, an AFM may work in contact or tapping mode. In contact mode, the tip is physically in contact with the surface i.e. it experiences prevalently short range repulsive forces. In contact mode, the vertical displacement of the tip, and then the force acting between the tip and the sample, is kept constant during the scanning. This operation is achieved using the feedback circuit. Before the scan starts, a set point, is chosen i.e. a deflection of the lever that will be kept constant during the imaging. For instance, if the tip encounters a high feature on the sample surface, the repulsive force increases, causing a bending upward of the cantilever. The feedback circuit compares the actual bending to the set point: if they do not coincide, it changes the voltage applied to the scanner to lower it so as to bring the deflection to the set point. In this operating mode the topography of the sample is built using the X-Y-Z movements of the scanner. Tapping mode is the AFM oscillating mode. The cantilever (Fig.3.6) vibrate in a periodic oscillating movement near its resonance frequency. Then the tip is brought close to the surface, at few nanometers of distance. At the lowest point of its oscillation the tip intermittently "touches" the sample. The interaction forces between the tip and the sample affect the oscillation of the cantilever. In order to image the topography of the sample, the feedback circuit keeps fixed the oscillation amplitude and, as for contact mode, the topography of the sample is built using the scanner movements. The two operation modes are illustrated by the graphical representation of the interaction potential energy between tip and sample U_{ts} shown in figure 3.6.

$$F_{ts} = -\frac{\partial(U_{ts}(z))}{\partial z} \tag{3.4}$$

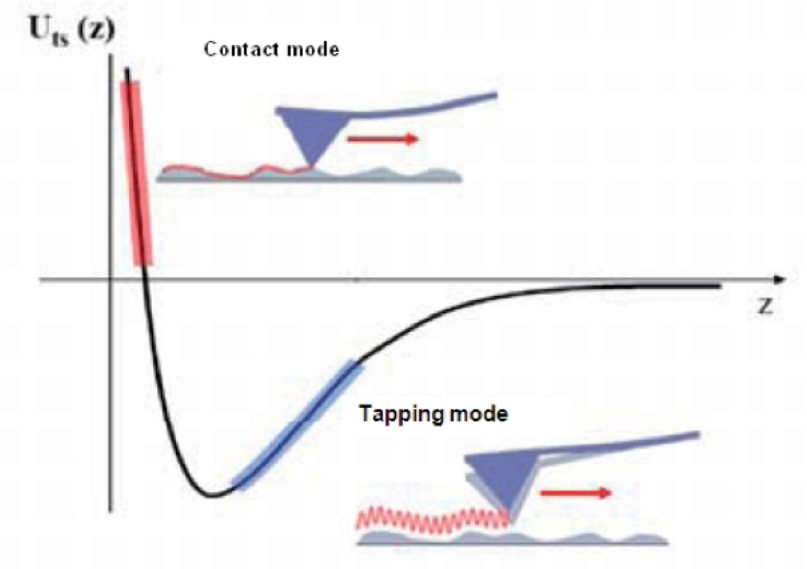

Figure 3.6: Schematic representation of the interaction energy between tip and sample as a function of their distance. Contact mode is generally characterized by a repulsive interaction, while tapping mode by an attractive one.

3.5.2 Force Spectroscopy Mode

Using an AFM in the force spectroscopy mode allows to obtain information of the forces acting between the two interacting surfaces. The force most commonly associated with the interaction between the AFM tip and the sample surface is the van der Waals force. The dependence of this force as function of the separation distance between the tip and the surface is illustrated in Fig. 3.7(a). The corresponding experimental record of the amount of force felt by the cantilever at a single location on a sample surface is depicted in Fig. 3.7(b), this is the so called force vs. distance (FD) curve. It gives information about the long range attractive or repulsive forces acting between the AFM tip and the sample surface, as well as about the mechanical and chemical local properties of the sample. Looking at the typical FD curve presented in Fig. 3.7(b), the approach and withdraw of the tip might be divided in four steps. In the first step, the piezoelectric scanner extends, letting the tip slowly approach the surface. At the beginning of this process, the AFM tip does not yet interact with the surface. There is neither a deflection of the cantilever, nor measurable force due to the large distance of separation between the tip and the surface. Then, while approaching progressively, attractive forces result in a small

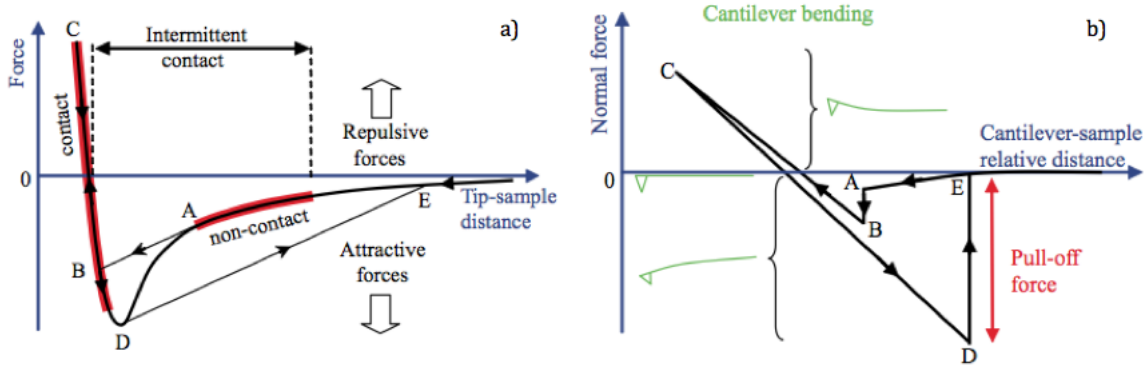

Figure 3.7: Schematic representation of attractive and repulsive forces experienced by the AFM-tip as a function of the tip-sample distance (a) and corresponding force distance curve giving information about the deflection of the front end of the cantilever (b).

downward deflection of the cantilever until the gradient of the attractive forces exceeds the elastic constant of the cantilever. At this point (A), the tip reaches an unstable position, resulting in a snap-into-contact of the tip on the surface (B). For the second step, the piezoelectric scanner continues with its expansion and the cantilever bends from a concave shape (attractive regime) to a convex shape (repulsive regime) with the tip in contact with the surface. The cantilever deflection is proportional to the movement of the piezo element assuming that the tip and the surface are rigid bodies. In fact, deformations are generally negligible compared to the cantilever deflection. This is of crucial importance to perform an accurate force calibration of the AFM, as we will discuss later. For the third step, the expansion of the piezoelectric scanner is stopped (C) while being in the elastic domain of deformation of the cantilever. And then, by contracting the piezo element, the withdraw of the tip begins. The tip stays into contact with the surface until the pulling force coming from the contraction of the piezoelectric scanner overcomes the tip-surface adhesion and results in the jump out of contact of the tip (D → E). The difference between the zero normal force and the force preceding the jump out of contact is called the pull-off force. The FD curve for the retracting process differs slightly from the approach part, on the one hand due to piezo hysteresis and, on the other hand, due to the tip-surface adhesion. The capillary forces, the increase of the contact area and short-range forces are the principal causes of the tip-surface adhesion.

A distinctive feature of force spectroscopy is its ability to quantify interaction forces as low as nano and even piconewton. However, calibration of the deflection sensor is necessary (i.e.

conversion factor of photodiode reading in V to nm) and must be done before any quantitative measurement can be performed for each cantilever used. The photodiode output for a given tip deflection can vary depending on exactly where the laser beam is reflected off the cantilever. The regular calibration procedure requires the acquisition of a force vs. distance curve on a hard substrate (mica was used during the course of the experiments presented in this thesis). Because of the stiff nature of mica, it does not deform and only the cantilever bends. Thus, the resulting cantilever deflection (which is proportional to the photodiode voltage) will be identical to the piezo-actuator displacement. Finally, the inverse of the slope of the force-distance curve at the contact region is a measure of the cantilever deflection sensitivity (measured in nm/V). Once the photodiode is calibrated, force vs distance in N vs μm can be acquired.

To calculate the sample elastic modulus, the Hertz model may be used. The Hertz theory predicts that the force increases non-linearly with indentation depth. Infact, from force vs distance curves information on the mechanical properties of the sample can be obtained applying the theory presented in section 2.3.2. According to the following mathematical relations for conical indenter

$$C_{T,conical} = tan(\theta), \;\; E_{R,conical} = \frac{2}{\pi}\frac{E}{(1-\nu^2)} \;\; and \;\; m = 2 \tag{3.5}$$

the force between a conical tip and a flat surface can be expressed as,

$$F_{conical\,tip} = \frac{2E\tan(\theta)}{\pi(1-\nu^2)}\,\delta^2 \tag{3.6}$$

while, for a spherical indenter are

$$C_{T,spherical} = R^{1/2}, \;\; E_{R,spherical} = \frac{4}{3}\frac{E}{(1-\nu^2)} \;\; and \;\; m = \frac{1}{2} \tag{3.7}$$

that leads to

$$F_{spherical\,tip} = \frac{4ER^{1/2}}{3(1-\nu^2)}\,\delta^{3/2} \tag{3.8}$$

where F is the loading force, E is the Young Modulus, ν is the Poisson ratio, δ is the indentation depth. For a spherical indenter, R is the sphere radius while θ represents half the opening angle for a conical indenter (fig. 3.8).

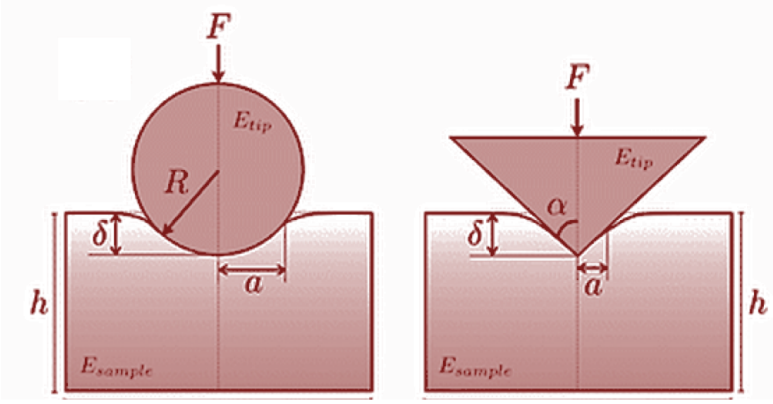

Figure 3.8: Schematics of the contact problem simulated in this work. The spherical indenter is described by a radius R, while the conical indenter is described by an half-opening angle α.

During the process to calculate the Young's modulus, the estimation of the indentation deep is required (equation 3.4) and thus the contact point of the force-distance curves has to be determined.

$$E = \frac{3(1-\nu^2)F}{4R^{1/2})}\,\delta^{-3/2} \tag{3.9}$$

An analysis of the equation 3.6 reveals that the precision in the determination of the contact point (and thus the determination of the indentation deep) can importantly affect the calculated E. If we take the derivative of this equation with respect to δ, and assuming the $\triangle\,\delta$ represent the error on determining the contact point, we get the follow identity,

$$\frac{\triangle E}{E} = -\frac{3}{2}\frac{\triangle\delta}{\delta} \tag{3.10}$$

Thus, for small indentations δ such as the ones observed when indenting very hard substrates, the right term becomes large and then the relative error $\triangle$E/E becomes large too. This means that only for large indents δ, the determination of the contact point will not substantially affect the determination of the Young's modulus and the limit for the validity of the Hertz model will depend solely on the material elastic limit.

Finally, from force vs distance curves information on viscoelasticity can be obtained. If the adhesion is negligible, the area enclosed between the approach and retract curves (loading and unloading) is related to the energy dissipated in the sample. Furthermore, since viscoelasticity depends on the loading/unloading rate the tip velocity can be varied to probe different viscoelasticity regimes and obtain quantitative data for hysteresis.

3.6 Data Analysis

Force spectroscopy experiments produce huge amount of data that requires a specific post-processing step to give comprehensive results. Since our AFM do not provide dedicated software to process this type of data, we developed our own software tools. The software, written in Matlab, automatically detects the contact point, extracts the Young's moduli and hysteresis values.

The program performs few steps that are highlighted in the following:

- at the beginning the force calibration curve is uploaded (fig. 3.9). This curve is acquired using mica as a sample and the same tip that will be used during the measurements on corneas. In the raw data format, a force curve has on the horizontal axis the piezo displacement expressed in micrometers and on the y axis the error signal, coming from the photodiode, expressed in Volts. The program automatically extract from the calibration curve the sensitivity value that is needed to convert the error signal from Volts to micrometers.

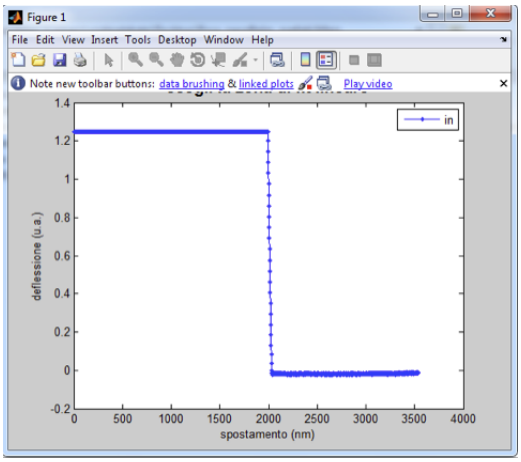

Figure 3.9: Force calibration curve.

- at this point, generic curves may be uploaded and automatically converted in force vs distance curves. The program will prompt for the manual input of the fit parameters: cantilever spring constant, opening angle of the conical tip and Poisson's ratio or radius of curvature of the spherical tip. Using the elastic constant value of the cantilever, the error signal value will be converted in Newtons.

- One of the key point of the program is the automatic detection of the contact point. The detection is performed on both the approaching and retracting curves. As an example, the first derivative of the approach curve is calculated and the contact point is chosen in the range where the derivative starts to be different from zero (fig. 3.10a). Both approach and retract curves are, then, shifted with respect to the calculated contact point (fig. 3.10b).

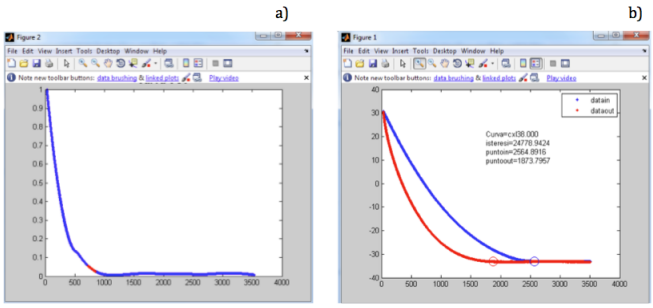

Figure 3.10: a) First derivative of the approach curve (in red the interval in which the contact point is located); b) approach and retract curves, circles point to the calculated contact points.

- The shifted approach curve is, then, used to determine the Young's modulus through a fit using the Sneddon model described in section 3.5 (Fig.3.11). For each curve, the fit range may be modified in order to improve the procedure.

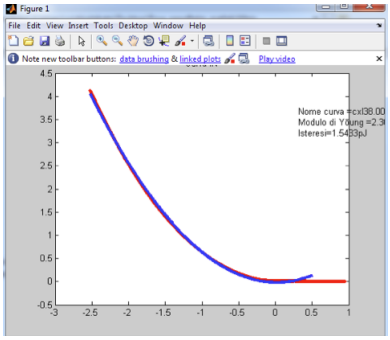

Figure 3.11: Sneddon model fit (blue) superimposed to the approach curve (red) for the calculation of Young's modulus.

Chapter 4

EFFECTS OF CXL TREATMENT ON CORNEAL BIOMECHANICS ON A NANOSCALE

As extensively reported in chapter 1, corneal CXL via UV-A irradiation of the cornea permeated with riboflavin, is an established procedure aimed at slowing down or halting the progression of keratoconus [54], [55], [56].

Several laboratory studies have been conducted to confirm the increase in tissue strength after CXL. Various techniques have been used, which included strip extensiometry, inflation testing of whole eye globes, Brilloun microscopy.

In recent years, AFM has been shown to reliably characterize the biomechanical properties of cornea either at the nanoscale and micrometer scale, including either the local elastic or viscoelastic characterization of the human corneal basement membranes, Bowman's layer, anterior and posterior stroma [61], [62], [63]. Recently, authors have demonstrated the valuable use of AFM to investigate the stiffening effect of riboflavin/UV-A corneal cross-linking [63], [64]. In this works, the cornea mechanical properties were measured with micro-metric probes.

For example, Young's modulus of elasticity for the anterior stroma was 245.9±209.1 kPa for the untreated control eyes and 467.8±373.2 kPa for the CXL treated eyes (fig.4.1) and Young's modulus for the posterior stroma was 100.2±61.9 kPa for the untreated control eyes and 66.0±31.8

kPa for the CXL treated eyes (Fig. 4.1).

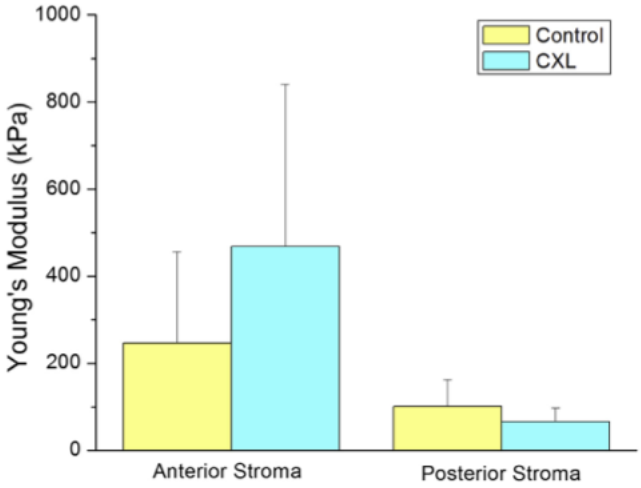

Figure 4.1: Bar graph of Young's modulus expressed in kPa for corneas that underwent collagen cross linking treatment compared to control corneas (no CXL), both for anterior and posterior corneal stroma.[64]

The scope of our study was to provide quantitative measurements of the biomechanical effect induced by corneal CXL on stromal collagen fibers using AFM.

4.1 Corneal Tissues

To develop and improve the experimental protocol 14 human corneas were used. All the specimen were obtained from the Veneto Eye Bank Foundation (Venezia Zelarino, Italy). All human tissues were used in compliance with the guidelines of the Declaration of Helsinki for research involving the use of human tissues. Once protocols were established, seven human sclero-corneal tissue were used for the experiments described in this section (see table 4.1). The sclero-corneal tissues were explanted between 10 and 19 hours after death and immediately preserved at 4°C in corneal storage medium enriched with 15% dextran, after gently removing the epithelium with a Merocel sponge (Medtronic, Minneapolis, MN, USA) soaked in deionised water. Corneal thickness and endothelial cell density were measured using an ultrasound contact pachymeter (UP-1000, Nidek Co. LTD., Gamagori, Japan) and an inverted optical microscope (Axiovert 25, Carl Zeiss Microscopy, Jena, Germany) respectively.

The corneal lenticules were divided in two groups: the first group of 5 specimens under-

Table 4.1: Characteristics of the eye bank donor corneal tissues

Group 1: riboflavin/UV-A corneal CXL Group 2: glutaraldehyde 2.5% CXL							
Approach speed (μm/s)	**Cornea #1**	**Cornea #2**	**Cornea #3**	**Cornea #4**	**Cornea #5**	**Cornea #6**	**Cornea #7**
Donor age (years)	69	70	69	69	53	68	63
Endothelial Cell Density (cells/mm^2)	2700	1900	2600	2200	2300	1900	2100
Central corneal thickness (μm)	501	547	507	545	520	537	561

went corneal CXL treatment, while the second group of 2 specimens underwent chemical cross-linking using a glutaraldehyde 2.5% solution. The corneal lenticules that were chemically cross-linked using glutaraldehyde 2.5% solution provided a reference to which compare the increase in stiffness after riboflavin/UV-A irradiation. The biomechanical properties of each specimen were measured before and after the cross-linking procedures. The riboflavin/UV-A cross-linking was performed as follows: each stromal lenticule was immersed in dextran-enriched 0.1% riboflavin solution (Ricrolin, Sooft Italia, Montegiorgio, Italy) for 30 minutes, under dim light conditions to avoid effects of incident light (Sondergaard et al). Before UV-A irradiation, the specimens were gently washed with balanced physiologic solution (BSS) in order to remove the excess of riboflavin. Each corneal lenticule was then irradiated with UV-A (370±8 nm) for 30 minutes, while riboflavin solution was instilled every 5 minutes, with an irradiance of 3 mW/cm^2. The UV-A delivery system (Vega, CSO, Italia) was located 56 mm from the corneal surface. An irradiation area of 7.0 mm diameter was used. After UV-A irradiation the corneal lenticules were kept in 20% dextran solution at 4°C overnight. The second group of corneal lenticules was immersed in glutaraldehyde 2.5% solution for 30 minutes. After gently washing the lenticules with BSS, they were analyzed by AFM immediately after the treatment. The sample holder, built using a 3D printer, has a convex shape at its center (fig. 4.2a) that follows the curvature of the corneal tissue. This shape allows to easily accommodate the sample in such a way as to reduce the displacement during the interaction with the AFM tip. All AFM measurements were made with the tissue gently placed on the sample holder. No glue is used to attach the sample to the sample hopder, to preserve its mechanical properties.

4.2 AFM Data Acquisition

Before commencing the experiment, each sclero-corneal tissue was immersed in 20% Dextran solution for 90 min, at room temperature, in order to restore corneal thickness to physiological

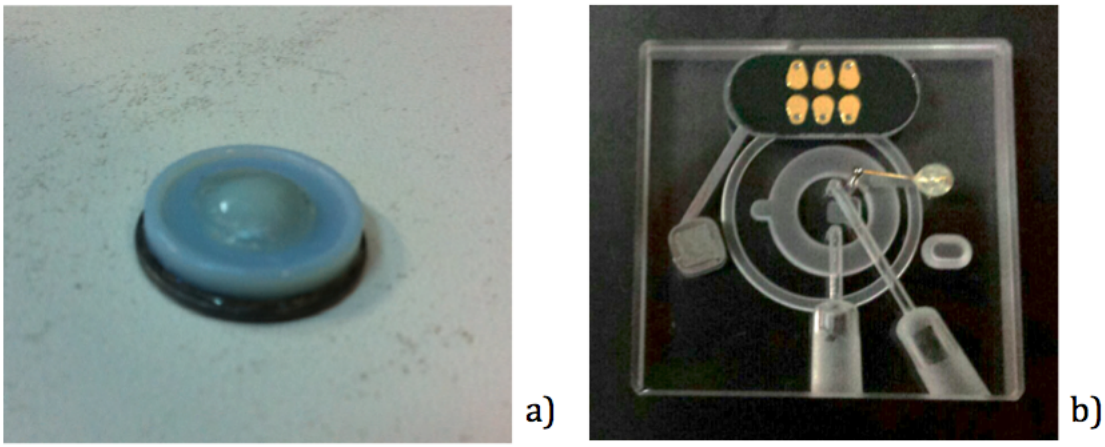

Figure 4.2: Sample holder (a) and fluid cell of the Nanoscope III AFM (b).

levels. Each sclero-corneal was then excised using a Barron punch (Coronet Graft, Coronet) in order to obtain 8.0 mm diameter corneal lenticules.

We have investigated the corneal specimen surface in contact mode in a dextran solution using a fluid cell (fig. 4.2b). The anterior stromal surface shows a feltlike appearance, with numerous pores of various depths and dimensions (Fig.4.3), demonstrating typical Bowman's layer characteristics, the mean RMS roughness is 102±7 nm.

Mechanical properties of the tissue were measured using a NanoScope IIIa Atomic Force Microscope (Veeco-Bruker) in the Force Spectroscopy mode [61], [65]. Measurements were performed at 27°C using as imaging medium a 20% dextran solution and phosphorus doped rectangular silicon cantilevers of nominal elastic constant between 20- and 80-N/m (TESPA, Bruker). Dextran was used as imaging medium to keep the tissues at the same osmolarity before and after corneal CXL using 20% dextran enriched riboflavin solution. The nominal value of the tip radius of curvature was 10 nm. This choice allowed us to investigate the sample on areas that were comparable with the dimension of the single collagen fiber. Force curves were obtained on different locations at the center of the stromal surface of each sample and hundreds of force curves (30 curves for each rate) were recorded at four different tip-velocities: 1.76 μm/s, 3.53 μm/s, 8.23 μm/s, 12.34 μm/s at each location.

No adhesion between the tip and the sample surface was detected in any sample. We made sure to avoid any possible alteration of the tissue during measurement; any rupture in the material would have induced a discontinuity in the force curve profile and therefore would have

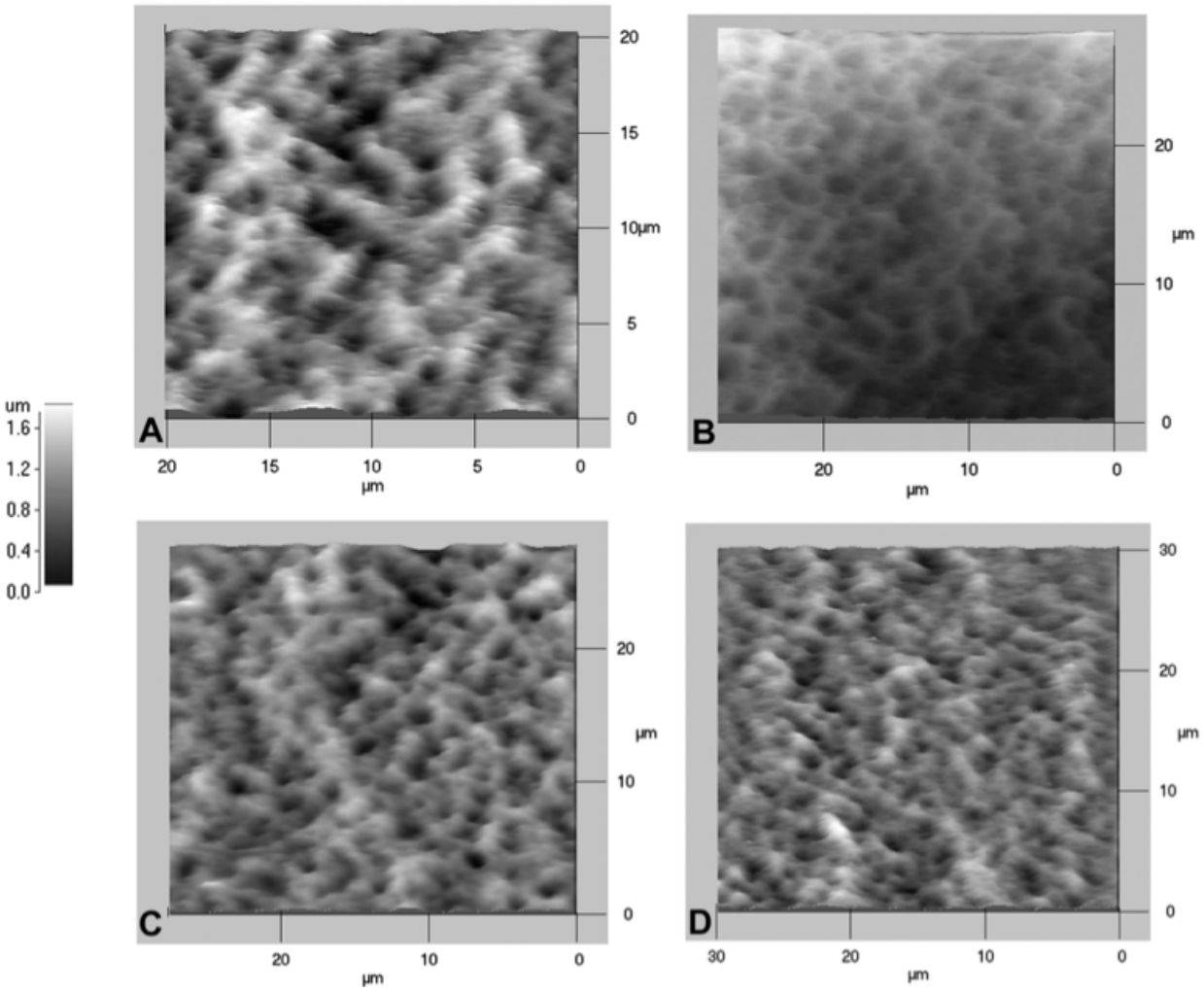

Figure 4.3: AFM images of the anterior stromal surface of a corneal samples (A; image size, 20 X 20 μm), 2, 3, and 4 (B, C, and D; image size, 30 X 30 μm). In the map, dark shades correspond to low features and light shades to high features. The vertical range of the displayed data is shown to the left of the images. The anterior human stroma demonstrates a feltlike architecture with micrometric pores of various sizes and dimensions. This morphology is thought to provide an interface for cell substratum interaction and for the diffusion of components or for the passage of the nerves into the overlying epithelial layers. The topography of Bowman's layer shows differences between samples that may imply structural internal differences in the micro-architecture of the anterior stroma. The size and density of anterior collagen fiber bundles and the underlying substrate may strongly influence the mechanical response of the anterior stroma.

been clearly seen. To optimize the measurement protocol various force curves using levers with different elastic constants were acquired. In particular, levers with the following elastic constants have been used 0.06N/m, 5N/m and 20-80N/m. Levers with an elastic constant of 0.06 N/m have proven to be too soft for the study of corneal samples. We note, in fact, from fig. 4.4.a and 4.4.b that adhesion forces are considerable. Curves obtained with stiffer levers show less adhesion between the tip and the sample and makes it easier to use the most common theoretical models describing the phenomenon for the interpretation of the results.

The AFM data interpretation requires the correct calibration of both the AFM optical sensitivity and the spring constant of each cantilever. Both the Young's modulus of elasticity (E) and the hysteresis (H) of each corneal sample were calculated individually before and after cross-linking. The Young's modulus was calculated using the Hertz-Sneddon model for a conical indenter [65], [66], [67]. Our custom software permitted to identify automatically the contact point and thus to provide a reproducible value of E, as previously shown [65]. Hysteresis was calculated as the area encircled between the extending and retraction curves. A typical force curve acquired when probing the anterior stroma with a nanometer-sized tip is schematized in figure 4.5, a typical extension-retraction cycle obtained in this study.

The absence of jump- to-contact indicates negligible interactions of the tip with the surface in dextran solution. The approach and retraction curves do not overlap, this phenomenon is due to the material's hysteresis. On retraction, the absence of a pull-off jump of the tip from the sample's surface is typical of viscoelastic materials.

4.3 Young's Modulus

Young's modulus was calculated from all the set of curves for all the specimen and different velocities. Figure 4.6 shows E values, as extracted from sample #1 curves acquired at 3.5 μm/s tip velocity, as a function of the maximum applied load.

Interestingly, E is almost constant over a range of applied loads, as it happens for linear elastic materials and there is an evident increase in Young's modulus following CXL treatment.

In all native corneal lenticules, the Young's modulus increased with increasing application rates, as summarized in table 4.2.

After riboflavin/UV-A CXL, the Young's modulus on average increased between 1.1 and 1.5 times with respect to baseline values in all tissues (fig. 4.7), except for sample #4 at an approach

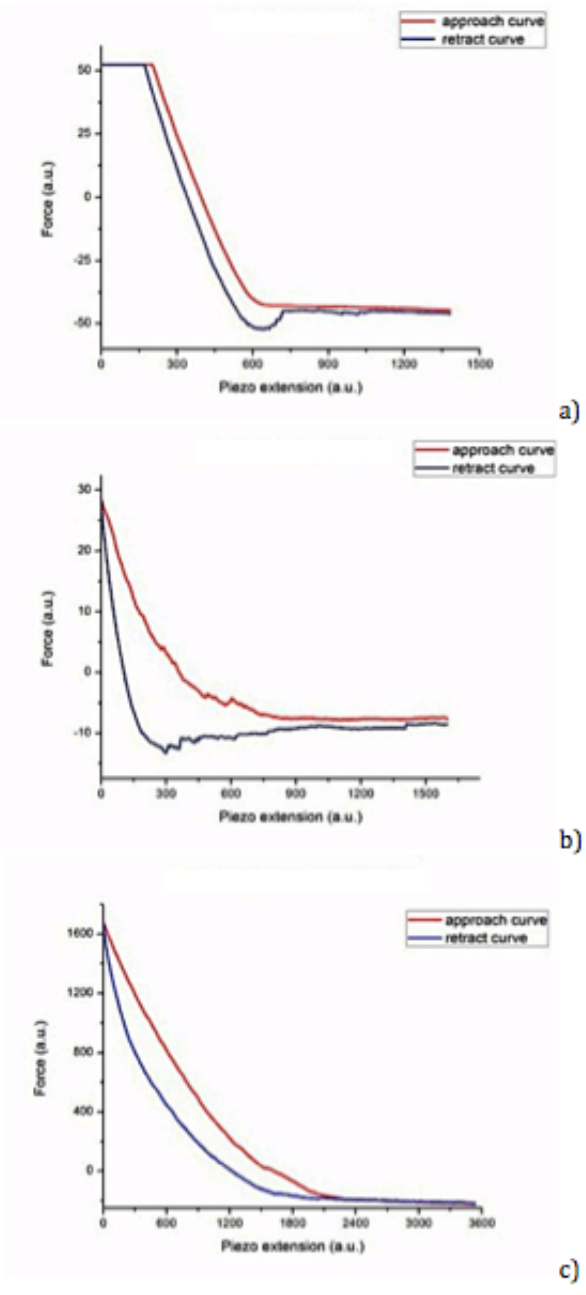

Figure 4.4: Force curves obtained on a corneal sample using levers with spring constant 0.06N/m (a), 5N/m (b), 20-80N/m (c), respective.

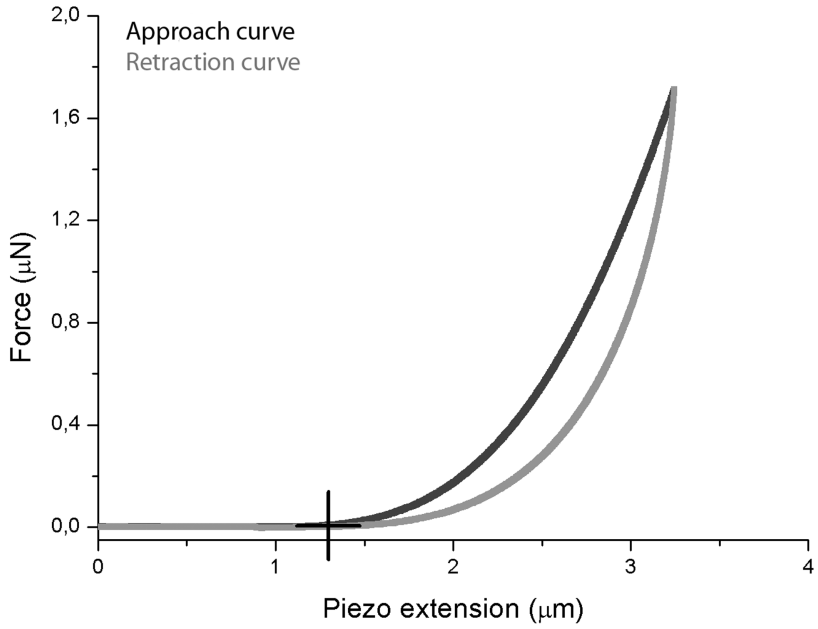

Figure 4.5: Sketch of a typical force-displacement curve using nanometer-sized tip. The black curve shows the force experienced by the tip when approaching the sample, while the grey curve represents the force experienced on retracting from the sample.

Table 4.2: Young's modulus (E; MPa) obtained for each sample before and after cross-linking (CXL)

			E values before riboflavin/UV-A CXL				E values before Glutaraldehyde CXL
Approach speed (μm/s)	**Cornea #1**	**Cornea #2**	**Cornea #3**	**Cornea #4**	**Cornea #5**	**Cornea #6**	**Cornea #7**
1.7	1.48±0.17	2.80±0.22	1.14±0.20	2.87±0.12	4.77±0.79	1.28±0.13	5.38±0.21
3.5	1.68±0.20	3.01±0.23	1.15±0.36	3.41±0.16	6.09±1.04	2.00±0.14	6.59±0.06
8.2	2.02±0.20	3.48±0.32	1.48±0.48	4.49±0.32	7.94±1.00	3.29±0.02	9.38±0.62
12.3	2.22±0.29	3.78±0.36	2.27±0.47	5.34±0.55	10.19±1.06	4.10±0.07	10.88±1.25
			E values after riboflavin/UV-A CXL				**E values after Glutaraldehyde CXL**
Approach speed (μm/s)	**Cornea #1**	**Cornea #2**	**Cornea #3**	**Cornea #4**	**Cornea #5**	**Cornea #6**	**Cornea #7**
1.7	2.21±0.42	3.26±0.20	1.62±0.34	3.82±0.37	7.46±0.15	5.10±0.18	10.81±0.36
3.5	2.54±0.29	3.59±0.14	1.63±0.33	4.12±0.32	9.11±0.21	5.61±0.17	11.50±1.26
8.2	2.98±0.62	4.03±0.18	2.13±0.41	4.69±0.18	12.44±0.50	6.31±0.01	11.39±1.23
12.3	3.28±0.59	4.21±0.32	2.77±0.40	5.04±0.13	16.09±1.19	7.00±0.01	12.20±0.85

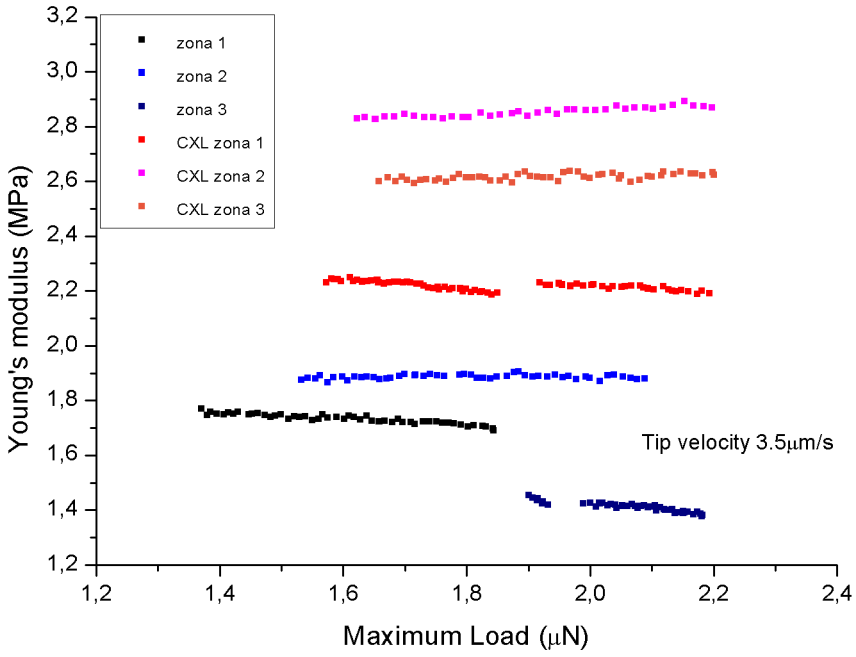

Figure 4.6: Plot of the Young's modulus (E) as a function of the maximum applied load.

speed of 12.3 μm/s (table 4.2).

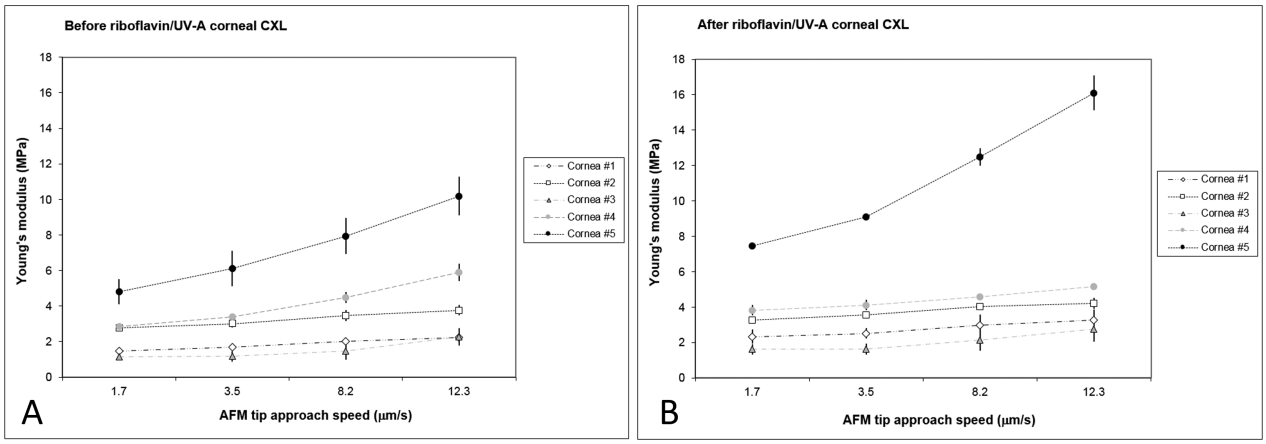

Figure 4.7: A) Average values of the Young's modulus before riboflavin/UV-A CXL in all five corneal specimens. B) Average values of the Young's modulus after riboflavin/UV-A CXL. Bars indicate standard deviation.

With this exception, the increase of E was statistically significant ($P < 0.05$) at all application rates in all tissues. Representative force curves obtained before and after riboflavin/UV-A CXL are shown in fig. 4.8.

After chemical cross-linking with glutaraldehyde, the E values averagely increased between 1.5 and 2.6 times with respect to baseline values (table 2). The increase was greater than 2 times at the lower approach speeds (<8.2 μm/s) in both samples. The increase was less pronounced for high tip velocities at which the viscous behavior of the corneal specimen decreased (fig. 4.9)

4.4 Hysteresis

The changes of the viscoelastic properties of the anterior stroma induced by cross-linking were evaluated by comparing the measurements obtained at specific ranges of applied loads both before and after treatment in each specimen. This procedure permitted to compare the hysteresis values with respect to the applied load, rather than the indentation depth, that was expected to change after cross-linking due to tissue stiffening. Hysteresis data were extracted from a set of curves obtained from sample # 1 at a tip velocity of 3.5 μm/s and they are shown in figure 4.10. As expected, H values decrease after cornea underwent the CXL treatment

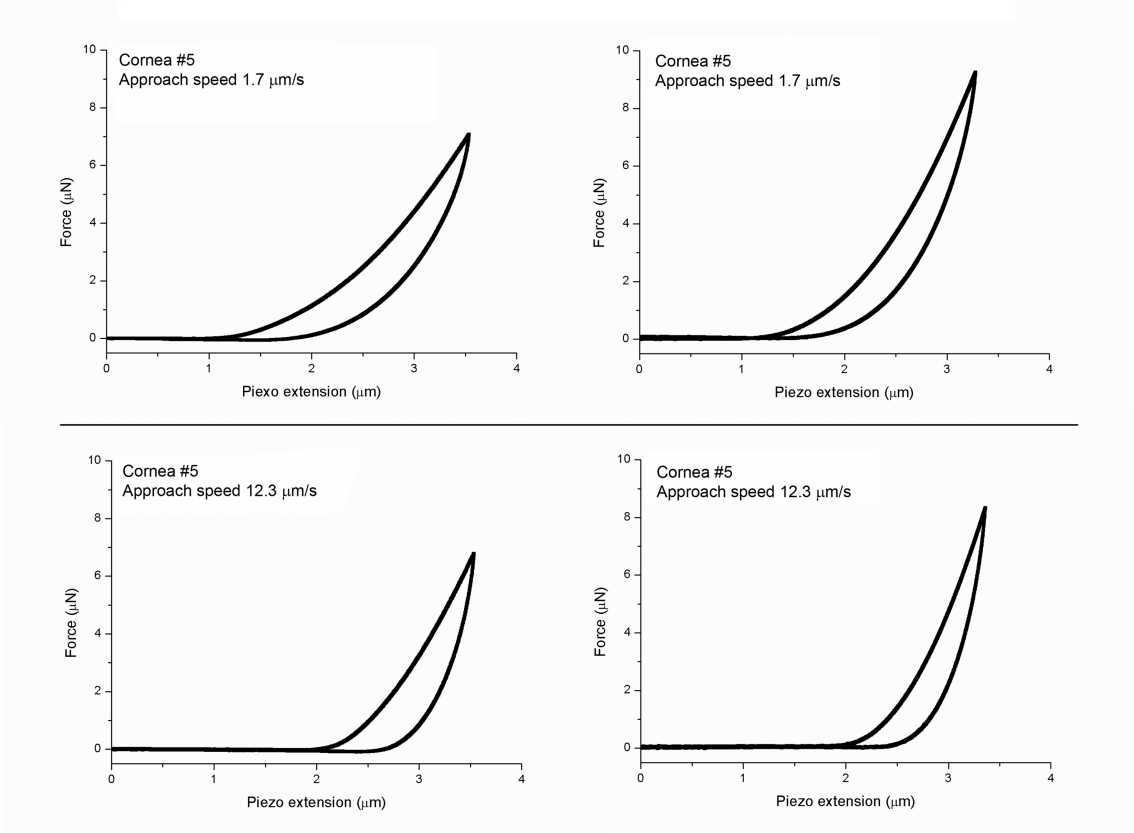

Figure 4.8: In cornea #5, the force curves were acquired at approach speeds of 1.7- and 12.3-μm/s both before (left column) and after (right column) riboflavin/UV-A cross-linking. After riboflavin/UV-A CXL, the approach curves become steeper, thus demonstrating a stiffened stroma; in addition, hysteresis decreases at the scale of stromal molecular interactions.

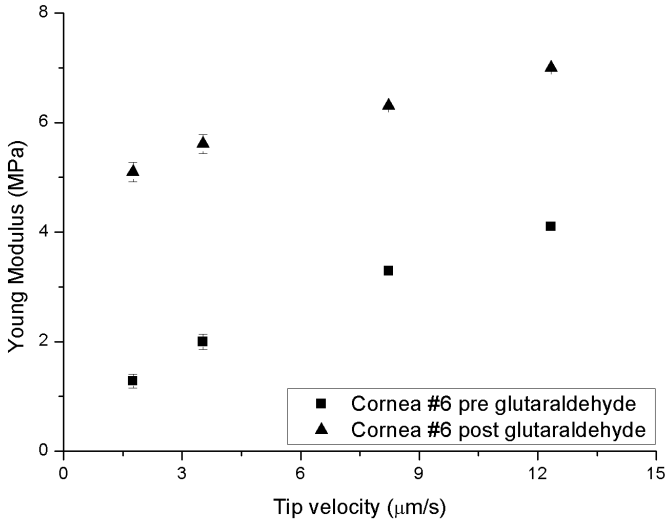

Figure 4.9: Young Modulus plotted as a function of the tip velocity before (squares) and after (triangles) treatment with glutaraldehyde. Bars indicate standard deviation.

The hysteresis and the indentation depth values acquired in all specimens that underwent riboflavin/UV-A CXL are summarized in table 3. Both the hysteresis and the indentation depth decreased after treatment in all tissues; the average decrease in H ranged between 0.9 and 1.5 times with respect to baseline values ($P < 0.05$). The highest decrease in hysteresis was found in cornea#1 (fig. 4.11a); the smallest decrease was found in cornea #2 (fig. 4.11b).

After riboflavin/UV-A CXL, the indentation depth decreased of 1.1-1.3 times than before treatment in all tissues. After chemical cross-linking using glutaraldehyde, we found a dramatic decrease of H in both specimens at all approach speeds, ranging between 2.6 and 3.5 times with respect to baseline values (figure 4.12). Accordingly, the indentation depth decreased of 1.2-1.6 times than before treatment.

4.5 Discussion

The efficacy of riboflavin/UV-A corneal CXL is primarily based on laboratory data demonstrating that the procedure increases the stiffness of the treated cornea. The effect of CXL on the mechanical properties of the cornea has been evaluated via different methods and techniques.

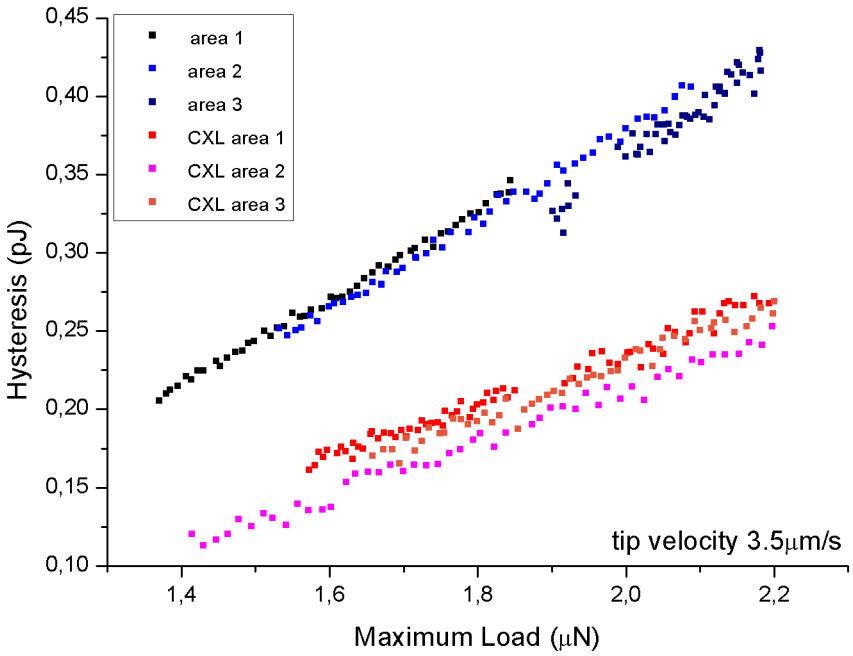

Figure 4.10: Hysteresis plotted as a function of the maximum applied load at the tip velocity of 3.5μm/s.

Table 4.3: Hysteresis and indentation depth values obtained at same ranges of applied loads before and after riboflavin/UV-A corneal CXL

Hysteresis (pJ)										
	Cornea #1 load range: 1.9±0.1μN		**Cornea #2 load range: 3.6±0.1μN**		**Cornea #3 load range: 1.4±0.1μN**		**Cornea #4 load range: 4.5±0.1μN**		**Cornea #5 load range: 6.7±0.1μN**	
Approach speed (μm/s)	Before CXL	After CXL	Before CXL	After CXL	Before CXL	After CXL	Before CXL	After CXL	Before CXL	After CXL
1.7	0.29±0.05	0.17±0.03	0.35±0.07	0.30±0.04	0.26±0.02	0.21±0.01	1.26±0.03	0.82±0.01	2.40±0.69	1.88±0.02
3.5	0.35±0.02	0.21±0.02	0.49±0.03	0.36±0.06	0.30±0.03	0.25±0.01	1.50±0.02	0.99±0.02	2.36±0.04	1.78±0.03
8.2	0.42±0.03	0.28±0.04	0.66±0.03	0.53±0.02	—	—	1.47±0.02	1.16±0.012	—	—
12.3	0.47±0.02	0.34±0.03	0.81±0.04	0.66±0.01	—	—	—	—	—	—
Indentation depth (μm)										
	Cornea #1 load range: 1.9±0.1μN		**Cornea #2 load range: 3.6±0.1μN**		**Cornea #3 load range: 1.4±0.1μN**		**Cornea #4 load range: 4.5±0.1μN**		**Cornea #5 load range: 6.7±0.1μN**	
Approach speed (μm/s)	Before CXL	After CXL	Before CXL	After CXL	Before CXL	After CXL	Before CXL	After CXL	Before CXL	After CXL
1.7	0.29±0.05	0.17±0.03	0.35±0.07	0.30±0.04	0.26±0.02	0.21±0.01	1.26±0.03	0.82±0.01	2.40±0.69	1.88±0.02
3.5	0.35±0.02	0.21±0.02	0.49±0.03	0.36±0.06	0.30±0.03	0.25±0.01	1.50±0.02	0.99±0.02	2.36±0.04	1.78±0.03
8.2	0.42±0.03	0.28±0.04	0.66±0.03	0.53±0.02	—	—	1.47±0.02	1.16±0.012	—	—
12.3	0.47±0.02	0.34±0.03	0.81±0.04	0.66±0.01	—	—	—	—	—	—

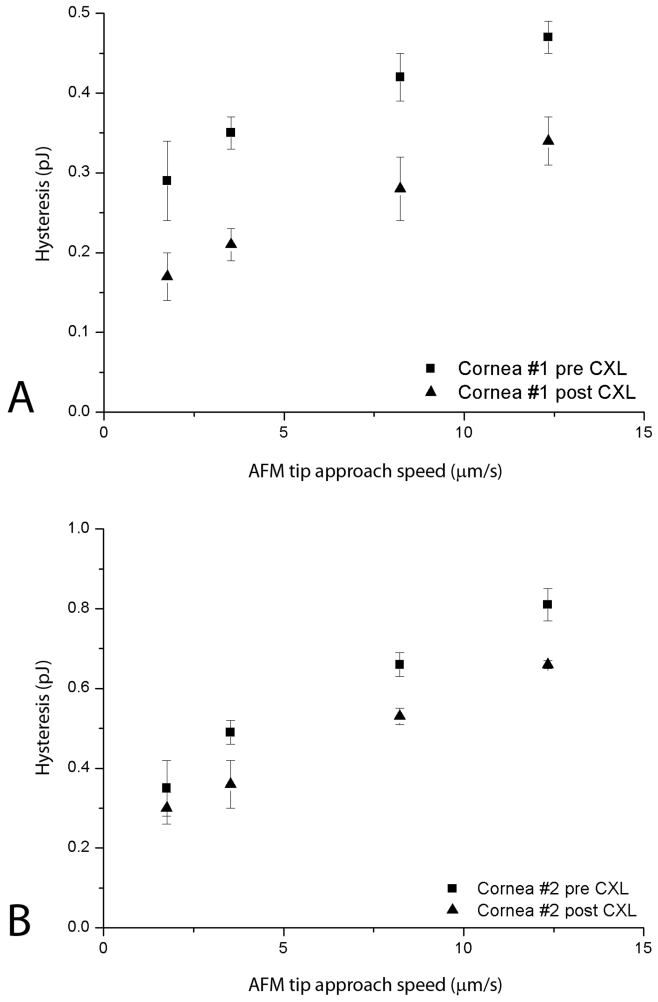

Figure 4.11: Hysteresis plotted as a function of the approach speed before and after riboflavin/UV-A CXL. A) Hysteresis of cornea#1 at the applied load of 1.9 μN. B) Hysteresis of cornea#2 at the applied load of 3.6 μN. The changes of hysteresis of the anterior stroma were evaluated by comparing the measurements obtained at specific ranges of applied loads both before (squares) and after (triangles) treatment in each specimen. Bars indicate standard deviation.

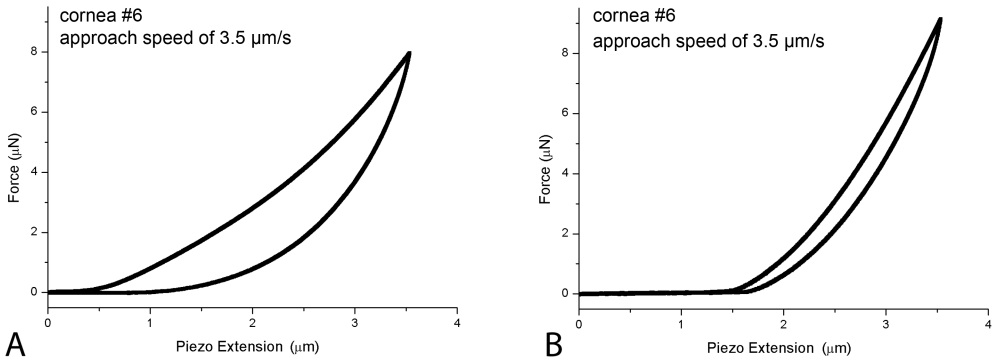

Figure 4.12: Representative force-displacement (F-D) curves before and after chemical corneal cross-linking using glutaraldehyde 2.5%. In cornea#6, the F-D curves were acquired before (A) and after (B) chemical cross-linking at an approach speed of 3.5 μm/s and an applied load of 6.5 μN. After treatment, the slope of the approach curve becomes steeper and the area under the curves becomes smaller than baseline measurements. The tip-stromal interaction demonstrates both an increase of the elastic response and a decrease of the viscous response of the stroma.

Inflation and strip extensiometry techniques provide a convolved measure of the modulus of elasticity of the corneal tissue, while additional cross-link bonds between stromal proteins have been found to occur mainly across the anterior half stroma. Thus, a stiffening gradient effect is expected from the anterior to the posterior stroma after CXL [10,11,13,25]. To assess the effect of riboflavin/UV-A corneal CXL locally, the biomechanical response should be measured across different layers of the cornea. Atomic force microscopy can measure the biomechanical properties of the cornea at different stromal depths with high accuracy [12-17]. In this study, a commercial AFM was used to probe the viscoelastic properties of the most anterior stroma of the human cornea. Each sample was compared independently from the others because of the inter-individual variation in biomechanical properties. Conical AFM tip with 10 nm radius were used to indent individually the stromal collagen fibers (30 nm width). The methodology permitted to indent the anterior stroma up to 2.8 μm depth, thus investigating the mechanical behaviour of the most anterior collagen bundles under the Bowman's layer. In addition, relatively high scan rates and loads were used in order to investigate the viscoelastic response of the tissue. A pair of tissues, that underwent chemical cross-linking using glutaraldehyde, were used as controls. Chemical cross-linking offers a direct method of identifying stable protein interactions. It is the ideal strategy for an unambiguous demonstration of protein-protein in-

teractions, in vitro. If two proteins physically interact with each other, they can be covalently cross-linked. Before treatment, the modulus of elasticity was rate dependent in all tissues, as previously discussed [15]. The larger elastic modulus found in our work with respect to previous AFM studies reflects mainly the modulus of the collagen fiber [15]. After riboflavin/UV-A CXL, the Young's modulus of the anterior stroma increased significantly in all specimens, except for cornea #4 at an approach speed of 12.3 μm/s. The post-treatment E values increased on average between 1.1 and 1.5 times with respect to baseline values at all scanning rates. After chemical cross-linking using glutaraldehyde 2.5% solution, the increase of E ranged between 1.5 and 2.6 times with respect to baseline values. This increase was higher at slow scanning rates, i.e., at the ranges where the nano-indentation response under loading was mainly determined by the elastic properties of the stroma [15]. In all native stromal samples, hysteresis increased with faster pressure applications, as previously found [15, 26, 27]. This rate-dependent behaviour is typical of viscoelastic biological tissues. After riboflavin/UV-A CXL, stromal hysteresis decreased in all samples; this decrease ranged between 0.9 and 1.5 times with respect to baseline values. A great decrease in hysteresis, ranging between 2.6 and 3.5 times with respect to baseline values, was found after chemical cross-linking using glutaraldehyde 2.5% solution. Recently, AFM has been used to evaluate the changes of the elastic properties of porcine and human corneas after riboflavin/UV-A CXL [13,14]. Dias et al. [13] used micrometer-sized (59-74 μm diameter) spherical indenters and 10.4 N/m cantilever to probe the stroma at different depths. The Authors used an approach speed of 15 μm/s with a maximum indentation depth of 6 μm, showing that the anterior stiffened significantly after CXL, while the posterior stroma did not. Seifert et al. [14] used a 0.98 μm radius spherical tip and 4.01 N/m cantilever to indent sagittal stromal cryosections with a thickness of 16 μm. Overall, the results from previous AFM studies have provided quantitative information on the depth-dependent profiles of the Young's modulus, showing that the stiffening effect of CXL is mainly limited to the anterior 220 μm stromal depth. Type I collagen is the most abundant structural component in corneal stroma. It is composed of three polypeptide chains and two types of single chains, α1 and α2, both of which are accessible to polymerization. Dimers of α chains are called β-components; trimers of α chains are called γ-components [28]. Glutaraldehyde (GA) cross-linking of the cornea has been shown to increase the area associated with each corneal collagen molecule (intermolecular spacing) by 11% [26, 29]. This observation can be a consequence of the type of polymerization induced by GA in collagen tissues. Glutaraldehyde reacts with the free amine groups of lysine or hydroxylysine amino acid residues of the polypeptide chains to form Schiff

base intermediates from which several subsequent reactions may occur before a crosslink is formed [30,31]. Overall, the hydrolysable Schiff bases are stabilized by further reactions with other GA molecules during the formation of crosslinks, therefore GA introduces free aldehyde groups to the fixed tissue. On the contrary, riboflavin/UV-A cross-linking does not involve any addition of molecular residues; this is in fair accordance to what shown by Hayes et al. [7]. The Authors, by using X-ray scattering, demonstrated that riboflavin/UV-A corneal CXL does not produce any significant change in the average fibril diameter or intermolecular spacing. However, the fibril spatial order factor was significantly higher in the cross-linked corneas when compared to untreated porcine corneas. The Authors have postulated that the increase in short range order of collagen fibrils following riboflavin/UVA CXL treatment might occur as a result of cross-links being formed within the fibril coating, i.e., within and between proteoglycan core proteins. In accordance with this hypothesis, Zhang et al. [6] have demonstrated a preferential formation of covalent bonds between collagen, decorin and mimecan. Riboflavin/UV-A corneal CXL could involve cross-linking of collagen molecules with themselves, proteoglycans (PG) core proteins with themselves and collagen molecules with the two specific PG core proteins, mimecan and decorin. Thus, in vivo the formation of additional cross-linking bonds between collagen molecules and PG core proteins may contribute substantively to increase tissue strength. In our work, we aimed to understand the biomechanical effect of the procedure at the scale of stromal molecular interactions and demonstrated both an increase of the Young's modulus and a decrease of hysteresis. These results are consistent with the formation of additional cross-linking bonds between stromal PG core proteins and collagen in riboflavin/UV-A corneal CXL. Adequate control on tissue thickness before and during biomechanical experiments has been shown to provide predictive results on the corneal behaviour [12,15,32,33]. Tissue thinning is the main macroscopic tissue change after stromal soaking with dextran enriched riboflavin administration, even prior to UV-A irradiation, because of the high solution hyperosmolarity. Previous work [34] has shown a relative decrease in stromal hydration of bovine corneas of 5.5% and 8.5% after 20% dextran riboflavin only and CXL treatment respectively. With decreasing corneal hydration the Young's modulus may increase [32]. This phenomenon can be explained based on the microstructure of the stroma. As the tissue thickness becomes smaller, the distance between negative charges become smaller and the net negative charge density inside the tissue increases. Therefore, decreasing the tissue thickness results in measuring a higher compressive force [35]. To avoid any bias due to changes in the hydration state during experiment, the corneal tissues were kept in 20% dextran

solution before riboflavin soaking and after UV-A irradiation. Based on the studies of Hamaoui et al. [36] and our previous work [12,15], it was found that 20% dextran solutions were effective in avoiding tissue swelling and maintaining corneal hydration during experimentation. In addition, only stromal soaking with 20% dextran enriched riboflavin solution was unable to increase the stiffness of the stroma [11,37]. In this study, we indented less than 3 μm of the most anterior stroma (on average 6% of the whole stromal thickness); the change of hydration was therefore considered negligible. In conclusion, we provided the first evidence that riboflavin/UV-A corneal cross-linking induces both an increase of the elastic response and a decrease of the viscous response of the stroma at the scale of stromal molecular interactions. These results are consistent with the knowledge that the formation of additional cross-linking bonds may occur at preferred sites of the surface of collagen fibrils and PG core proteins.

Chapter 5

BIOMECHANICAL ANISOTROPY OF THE HUMAN CORNEAL STROMA

The mechanical properties of the stroma define for the most part the mechanical properties of the whole tissue. The normal human corneal stroma has shown regional differences in the histology which reflects in structural anisotropic biomechanical properties. Studies of the microstructure of the cornea demonstrated the highly heterogeneous nature of the stroma. In the normal human stroma, the collagen fibrils have a different orientation depending on the specific region and corneal layer being evaluated. Microscopy investigations clearly indicated that the bundles of collagen fibrils are preferentially oriented in one direction peripherally (circumferentially, near the limbus) or two directions centrally (inferior-superior and nasal-temporal), thus giving rise to a grid-like structure. This arrangement is more regular in the posterior stroma than in the anterior stroma. Within an individual lamella (each lamella run uninterruptedly from limbus to limbus, with a variable diameter according to the stromal depth and 2 ± 0.5 μm thickness), the collagen fibrils form a regularly packed parallel array that follows the direction of the lamella, except where branching of a lamella occurs. Transverse branching is mostly observed in the anterior third part of the stroma. Each collagen fibril has a mean diameter of 30 ± 5 nm; the interfibrillar spacing s 50 nm in the corneal center and 65 nm in the corneal mid-periphery: therefore, collagen fibers are more closely packed in the center of the cornea than in the midperiphery. Further, the anterior central stromal lamellae appear to be more closely packed than other regions of the cornea with high stiffness and a

main importance in maintaining the corneal strength and hence its curvature. In relation to these anatomic regional differences, there are also regional biomechanical differences. The various parts of the human cornea strain differently when exposed to the same intraocular pressure load. The differences in regional corneal strain may either be due to a real difference in corneal elasticity or to regional differences in the corneal stress level. The anterior stroma is less hydrated than the posterior stroma and appears to be stiffer than the latter with stronger junctions between collagen lamellae. Interlamellar cross-links, which are preferentially distributed in the anterior one third and periphery of the stroma have been postulated to contribute to the regional differences in lamellar shearing strength and interlamellar cohesive strength in the human cornea. The deeper stroma has been measured to have less strength and less resistance to swelling compared to anterior stromal layers.

Several different methods have been used to determine the bulk elastic modulus of the cornea (a value that integrates over all layers of the cornea) and a wide range of values has been published (0.01-11.1MPa). The main investigation methods were tensile testing and bulge testing which are not suitable for determining the elastic modulus of each discrete corneal layer.

Last et al. have published a study on the mechanical properties of the Bowman layer and the anterior stroma [68]. Previously the same authors have reported on the elastic modulus of the anterior basal membrane and the Descemet membrane of the human cornea. Their results have shown that the elastic moduli of each layer of the cornea are unique and play a fundamental role in maintaining the homeostatic balance of the eye.

5.1 Tissue Preparation

Experiments were carried out on human donor corneas (age range: 19-92 years) retrieved from the Florida Lions Eye Bank (Miami, FL). The human eye globes arrived from the eye bank in sealed vials placed in Styrofoam containers filled with ice. The whole globes remained in the 20% Dextran solution (20 g of Dextran in 100 mL of PBS; D8821, avg. molecular weight: 64,000e 76,000 g/mol, Sigma Aldrich, St. Louis, MO) for 24 h in the refrigerator at 4(grade). Pachymetric measurements were taken using an ultrasound pachymeter (DGH 55 Pachmate, DGH Technology Inc., Exton, PA) after 24 h to ensure the restoration of the corneal thickness within the physiological range of 400-600 mm.

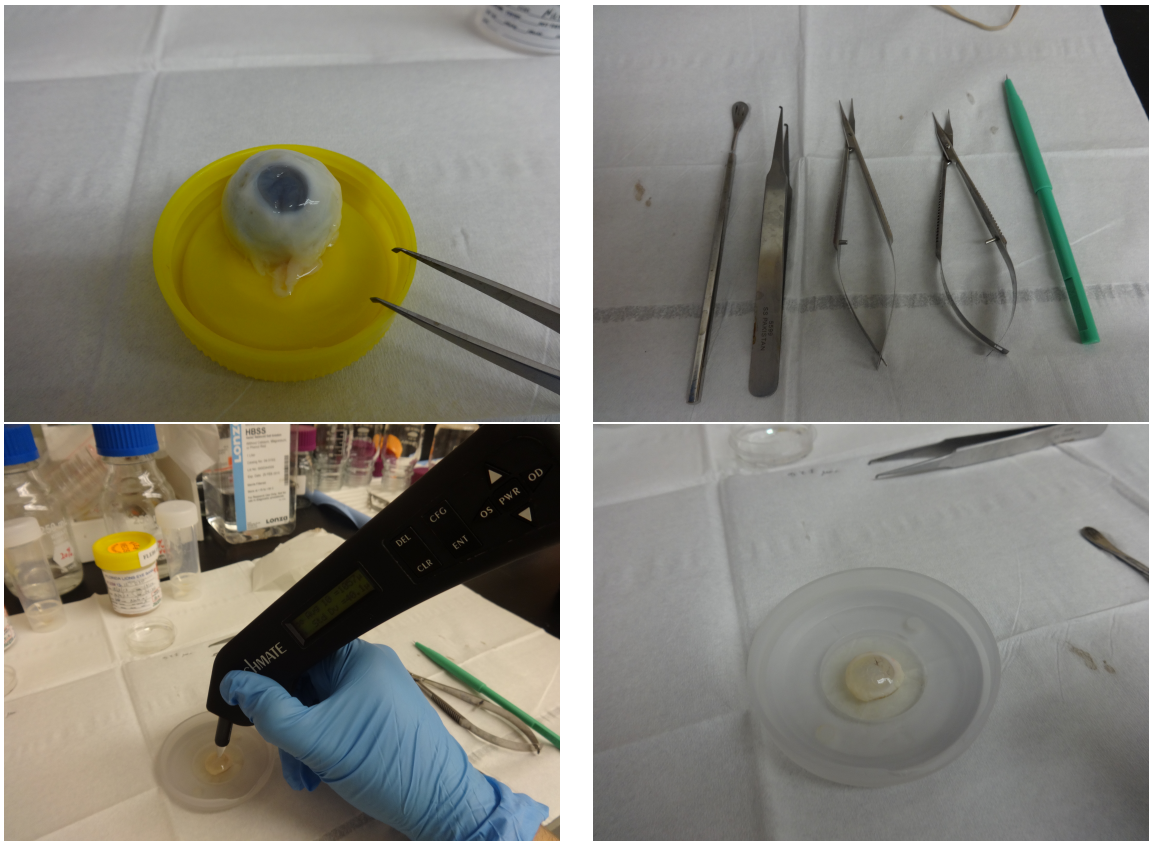

Figure 5.1: (a) Human eyeball. (b) Tools for preparing corneal specimen. (c) Pachymeter (DGH 55 Pachmate, DGH Technology Inc., Exton, PA) used to measure corneal thickness. (d) Human cornea housed on the sample holder.

Each cornea was excised within the sclera beyond the limbus and was mounted on a custom cornea holder (Fig.5.1). The holder is characterized by a spherical protrusion that has a radius of curvature matching the corneal one. Thereafter, each sample was mounted onto an artificial chamber and a microkeratome (CB, Moria) was used to section the cornea into an anterior and posterior lenticule. Two different heads, 50 μm and 90 μm, were used.

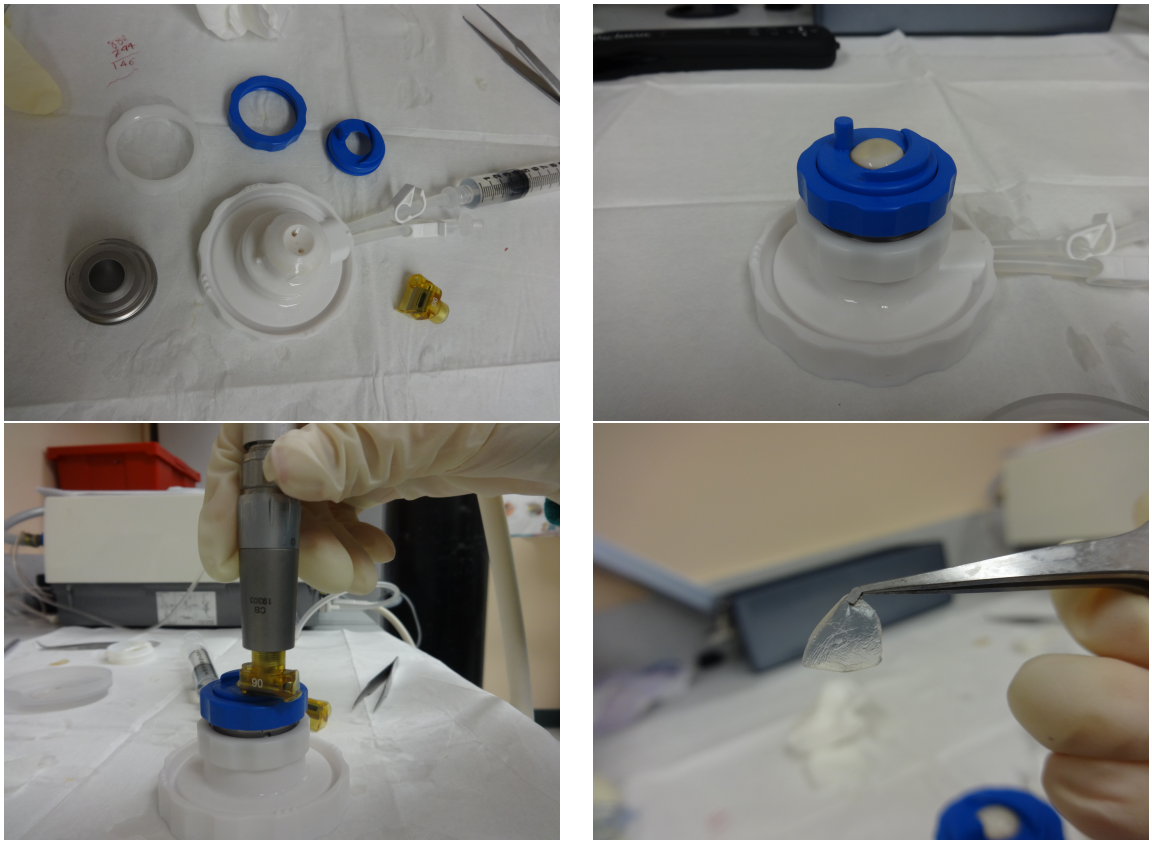

Figure 5.2: (a) Components of the microkeratome (CB, Moria). (b) Cornea placed into the sample holder maintained at a pressure of 766mmHg. (c) During the cutting. (d) Slice of corneal tissue.

5.2 AFM Measurements

Corneal specimens were placed in an AFM custom sample holder and maintained in place mechanically without the use of glue to preserve their mechanical properties, the custom cornea holder containing the sample was placed under the AFM cantilever (Fig.5.3).

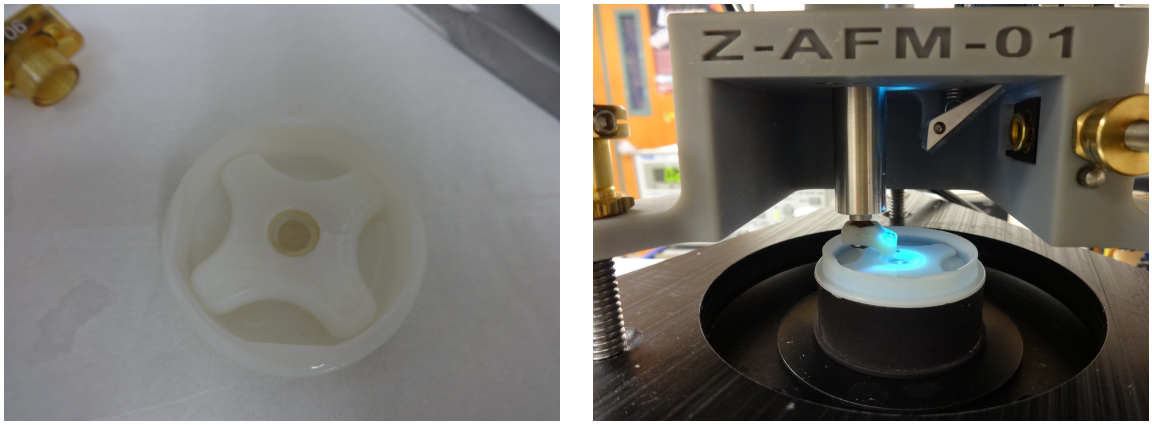

Figure 5.3: (a) Custom Cornea Holder. The holder is comprised of a spherical lens that has a radius of curvature matching the corneal one. The cornea was secured onto the spherical base with the holder's anchoring top that contains a hole to expose the central region of cornea for mechanical testing. This holder enables sturdy anchoring of an intact cornea, maintenance of corneal curvature, and the filling of 15% Dextran solution for proper corneal hydration during AFM testing. (b) Cornea holder placed under the AFM tip.

The sample was positioned so that the modified cantilever tip was over the central portion of the sample. The tip was lowered until it was just touching the surface. This position was determined by the point when the reflected laser beam moves off the photodiode. The location of the cantilever on the sample was observed using the 10X microscope objective connected to the camera beneath the sample. This enabled the positioning of the cantilever above an area with no surface irregularities. The modified tip was then lowered using the piezoelectric control so that it was in contact with the tissue [64]. The measurements were conducted using cantilever approach and retraction speeds of 15 μm/s and 2 μm/s. The voltage detected at the photodiode due to deflection of the cantilever was recorded as a function of piezoelectric displacement. These recordings were repeated at least 20 times per sample. All experiments were performed at room temperature.

Table 5.1: Data for donors' age, stromal depth and Young Modulus calculated for a spherical tip and a tip velocity of 15 μm/s.

Age	Stromal Depth (μm)	Young Modulus (MPa)
92	59	0.99±0.12
92	73	0.90±0.03
81	82	0.91±0.05
19	127	1.03±0.21
62	136	0.17±0.01
73	137	0.71±0.05
62	147	0.22±0.02
22	174	0.2±0.03
19	202	0.17±0.01
81	205	0.72±0.08
22	218	0.41±0.04

5.3 Elasticity as a Function of Stromal Depth

5.3.1 Spherical Indenter

Commercially available AFM tips are typically less than 50 nm in diameter, and are therefore limited to mechanical characterization of individual tissue constituents. To measure tissue-level mechanical properties of soft tissues using indentation testing, it has been determined that a contact area greater than 50 μm in diameter is required. With the intent of characterizing at the tissue-level, this part of the study used AFM cantilevers modified with 39μm glass microspheres. The use of modified cantilevers increases the surface contact area with the sample thereby enabling networks of the stromal tissue microstructure to be mechanically probed rather than individual collagen components of the stroma. As described in the previous chapter, we performed measurements on corneas in a dextran solution.

Dextran solution was used to restore corneas to their normal thickness range of 400-600 μm. Dextran has been extensively studied in the area of post-mortem corneal preparation and hydration for experimental studies, it was noted that Dextran solutions of 20% proved most effective in bringing edematous corneas back to normal in vivo thickness ranges and

that 15% effectively maintained corneal hydration during experimentation.

Experiments were performed on 11 human corneas (Table 5.1). The force curves were obtained on the surface of the posterior cut for a tip velocity of 15 μm/s. 20 curves for each different slice depth were recorded. Stromal depth refers to the thickness of the anterior lenticule. Each set of data was analyzed using the procedure described in 3.6 and the values of the calculated Young's modulus as a function of stromal depth are reported in table 5.1. A decrease in the Young's modulus is observed at increasing stromal depth as shown in figure 5.4, (range of E: 0.17-0.91 MPa).

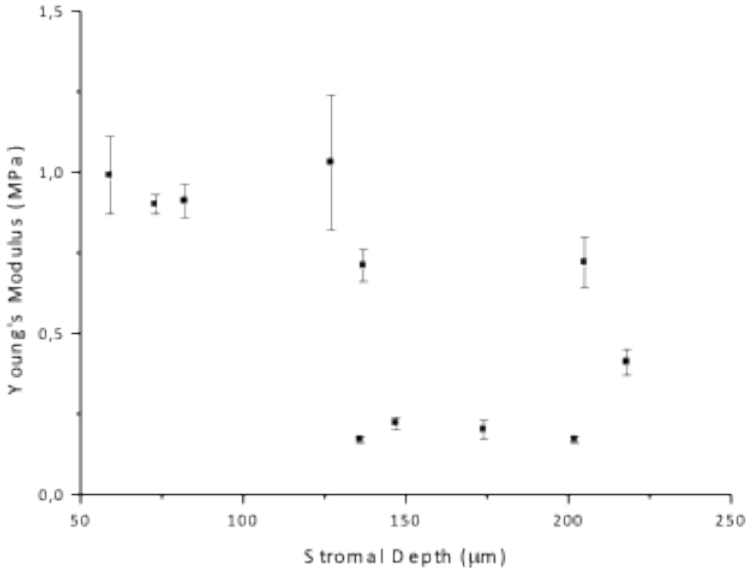

Figure 5.4: Young's modulus vs stromal depth, bar refer to standard deviation.

The decrease has a gradient behavior, Young's modulus has an almost constant value over the anterior 120 μm stromal depth their decreasing with increasing depth.

In 5 corneal samples, force vs distance curves were acquired at a tip velocity of 2μm/s. Data are reported in table 5.2. As for data extracted at higher tip velocities Young's modulus of elasticity significantly decreased as measured slice depth increased (range of E: 0.22-0.56 MPa) (Fig. 5.5).

The values of Young's modulus are smaller than the ones obtained from the curves acquired at higher velocity.

Table 5.2: Data for donors' age, stromal depth and Young Modulus calculated for a spherical tip and a tip velocity of 2μm/s.

Age	**Stromal Depth (μm)**	**Young Modulus (MPa)**
92	59	0.55±0.04
92	73	0.56±0.04
81	82	0.34±0.04
73	137	0.35±0.04
81	205	0.22±0.03

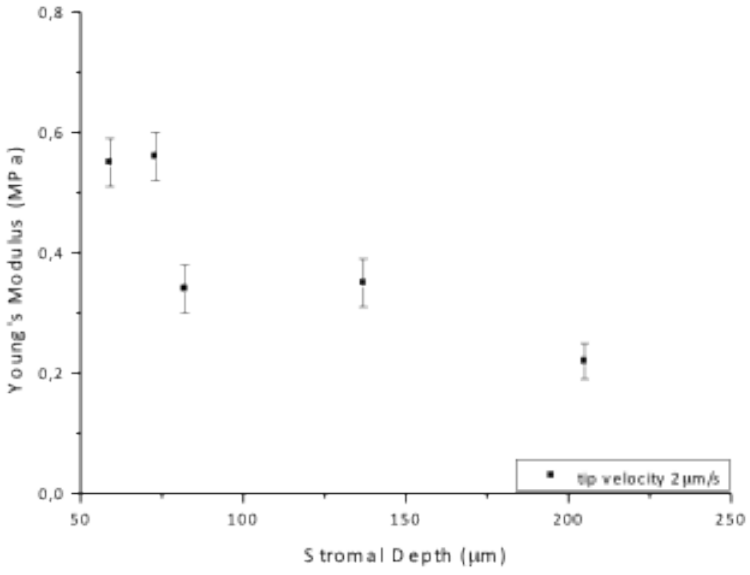

Figure 5.5: Young's modulus vs stromal depth, bars refer to standard deviation. Values refer to data acquired at 2 μm/s tip velocity.

Table 5.3: Data for donors' age, stromal depth and Young's modulus calculated for a conical tip and atop velocity of 15μm/s.

Applied load = 5.3 ±0.3μN		**Applied load = 7.3 ±0.3μN**	
Stromal Depth (μm)	**Indentation (μm)**	**Stromal Depth (μm)**	**Indentation (μm)**
82	1.75 ±0.17	73	2.14±0.11
147	4.22±0.33	137	2.78±0.27
		136	4.97±0.29
		202	5.34±0.17

Table 5.4: Data for donors' age, stromal depth and Young Modulus calculated for a conical tip and a tip velocity of 15μm/s.

Age	**Stromal Depth (μm)**	**Young Modulus (MPa)**
81	81	3.99±0.63
19	127	2.87±0.61
73	137	2.94±0.43
81	205	2.57±0.26

Additionally, from force vs distance curves data on sample indentation can be extracted. Corneal indentation is strictly dependent on the applied load. Since it is difficult to keep the force between the tip and the sample constant, we have compared the indentation values at two well-defined loads for a tip velocity of 15μm/s. Data are collected in table 5.3.

For both applied loads, an increase in the indentation depths is recorded for increasing stromal depth. In particular, for an applied force of (7.3±0.3)μN around 130μm an abrupt change in the indentation is recorded.

5.3.2 Conical Indenter

Four corneal specimen were also probed using commercially available conical tips. The nominal tips radius of curvature was of 10nm and the cantilever elastic constant was 40N/m. In this case, as extensively described in the previous chapter, we were indenting the single collagen fibers.

We report a net increase in the Young's modulus, from hundreds of kPa to units of MPa,

with respect to spherical indenters. In table 5.4 are collected data about the donors' age, the stromal depth and the calculated Young's modulus from set of data acquired with a tip velocity of 15μm/s. Also in this case a decrease of the Young's modulus as a function of the increasing stromal depth is reported (Fig. 5.6). Values decrease from 4 MPa to around 300 kPa in a range 80-210 μm of stromal depth.

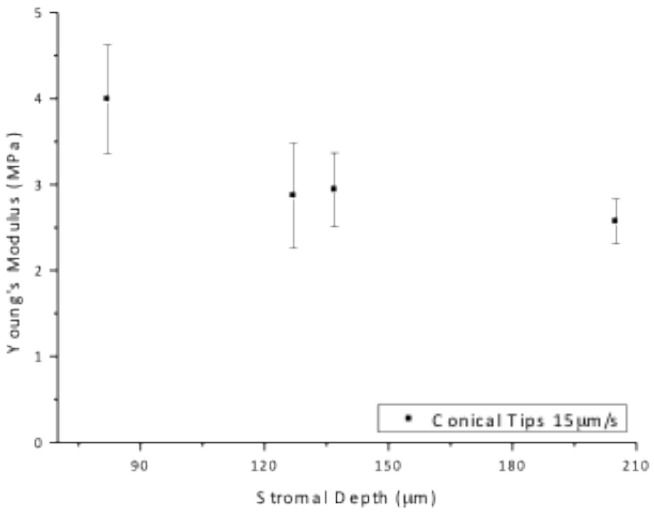

Figure 5.6: Young's modulus vs stromal depth

5.4 Discussion

The aim of the present work was to investigate the depth-dependent mechanical anisotropy of the human corneal stroma at the micro- and nano-level and to determine whether the biomechanics of the stroma involves any relationships between different scales of measurement. In this study, a custom built AFM was used to investigate the elastic properties of human corneal stroma using two different types of indenters: a spherical one with a radius of curvature of 30-50μm of microns and a conical one with a radius of curvature of 10μm nanometers. At tissue level we found a decrease of Young's modulus increasing stromal depth. In particular, the calculated values for a tip velocity of 15μm/s showed an abrupt change in E that, at a stromal depth around 120μm, became one third of the value calculated at smaller stromal depths. For

stromal depths in the range 50-100 μm, E was around 1MPa while at larger stromal depths it was around 0.3MPa. At 2μm/s tip velocities, the same behavior was observed but with a decrease in the Young's modulus to about half the value calculated at small stromal depths. These results were in perfect agreement with what it is known about the corneal stroma. As mentioned in previous chapters, at the microscopic level, the corneal stroma appears as an organized, dense, avascular connective tissue comprising collagen and proteoglycans (PGs - principally decorin and lumican). Biomechanically, the collagen and the PGs, which are bound to the collagen fibrils, providing tensile load resistance. The collagen fibril/PG aggregates are arranged into the basic mechano/anatomical unit of the stroma the lamella. Each lamella contains a highly-oriented array of collagen fibrils with their attendant PGs. Lamellar size varies considerably as a function of depth in the stroma with anterior lamellae (0.5-30 μm wide and 0.2-1.2 μm thick) generally smaller than those in the posterior stroma (100-200 μm wide and 1.0-2.5 μm thick). Fibrils in each lamella are parallel to each other except where lamella split or branch [70]. The microscopic organization of the stromal lamellae has significant implications for the biomechanical behavior of the cornea. In transverse section, the corneal stroma can be divided morphologically into an anterior third and posterior two thirds [69]. Figure 5.7 is an optical polarization micrograph which shows a striking difference in the lamellar organization. The anterior stroma exhibits substantial weaving of continuous lamellae in the anterior-posterior direction while in the posterior stroma, the lamellae run nearly exclusively in the plane of the cornea. The difference in the amount of anterior-posterior interweaving is likely to make the anterior human corneal stromal behavior mechanically-distinct with respect to the posterior human corneal stroma [35].

Based on the structure of the corneal stroma, it can be inferred that the anterior portion of the cornea is much stiffer than the posterior non-woven portion. This fact is supported by clinical and experimental studies, which show that the posterior two-thirds of the corneal stroma is easier to bluntly dissect in a lamellar fashion than the anterior third and that the anterior corneal curvature remains relatively constant at various physiological intraocular pressures and stromal hydration levels compared to the posterior corneal curvature. After induction of corneal edema in an ex vivo setting, ultrastructural studies by Muller at al. showed that the 10μm thick Bowman's layer and the underlying 100-120 μm of the stroma were the stiffest regions of the cornea. Quantitative ex vivo direct measurements of human corneal stiffness are very consistent with these observations. Uniaxial strip extensiometry demonstrates that the anterior third of the corneal stroma is 2-3 fold stiffer and stronger than the posterior two

Figure 5.7: Optical polarization micrograph showing the interweaving of the collagen lamellae in the anterior stroma and the planar organization of the lamellae in the posterior stroma. The arrow indicates the anterior stromal surface.

thirds [71]. Our results confirm this notion, and this is very interesting since AFM performs measurements in compression and not in extension. Few data show a slight deviation from the gradient behavior. This may be due to differences between human donors. The age and differences in stromal thickness may affect the calculated elastic modulus.

Conical AFM tips were used to indent individually the stromal collagen fibers. The larger elastic modulus found when using conical indenters reflects the modulus of the collagen fiber. Again a decrease of the Young's modulus at incresing stromal depth, as measured with a tip velocity of 15μm/s, is reported. The decrease can be related to the reduced number of cross link between the collagen fibers and the stromal proteins. It may also be related to the well known reduction of PGs in the posterior part of the stroma. Further, the reduction of E at incresing stromal depth is less evident than in the case of the spherical indenter. While for a spherical indenter the dependence of the Young's modulus from the stromal depth shows a step-like behavior, for a conical indenter the decay seems to follow a smoother path. The calculated values reveal that the magnitude of the decrease is less in the case of a conical indenter with respect to the conical one. It can be inferred that this difference is due to the size of the indentation area. Under a spherical tip a bigger amount of fibrils and cross links are compressed eliciting the mechanical response of a larger area of the stromal tissue, in which the influence of the non elastic components may play an important role. For a conical indenter, this contribution is negligible. More, in the anterior stroma there are more cross links and less water content so the elastic contribution is more important, while in the posterior part of the stroma GAGs are more hydrophilic with a consequent presence of bigger amounts of water.

Appendix A

Derivation of Sneddon Contact Mechanical Model

```
%% curve force vs indentation
k=str2double(dataconstant{1})*1e-9;
for i=1:length(force)
    indentation(i,1).indicecontatto=force(i,1).indicecontatto;
    length_in=length(force(i,1).datain(:,1));
    length_out=length(force(i,1).dataout(:,1));

    indentation(i,1).inx=
    (force(i,1).datain(:,1)-force(i,1).puntocontatto(1))*1e-3;

    indentation(i,1).iny=
    k*(force(i,1).datain(:,2)-min(force(i,1).datain(:,2)))*1e6;

    indentation(i,1).outx=
    (force(i,1).dataout(:,1)-force(i,1).puntocontatto(2))*1e-3;
    indentation(i,1).outy=
    k*(force(i,1).dataout(:,2)-min(force(i,1).dataout(:,2)))*1e6;
```

```
    indentation(i,1).scanrate=
    force(i,1).scanrate;
    indentation(i,1).name=
    force(i,1).name;
    indentation(i,1).caricomax=
    k*(mean([force(i,1).carico(1),force(i,1).carico(2)]))*1e6;
    indentation(i,1).isteresi=
    trapz(indentation(i,1).inx(1:indentation(i,1).indicecontatto(1),1),
    indentation(i,1).iny(1:indentation(i,1).indicecontatto(1),1))-...
        trapz(indentation(i,1).outx(1:indentation(i,1).indicecontatto(1),1),
        indentation(i,1).outy(1:indentation(i,1).indicecontatto(1),1)); end
%% Plot
for i=1:length(indentation)
    figure(3);
%     hold on
    h1=plot(indentation(i,1).inx,indentation(i,1).iny,'r.',...
        indentation(i,1).inx(indentation(i,1).indicecontatto(1)),
        indentation(i,1).iny(indentation(i,1).indicecontatto(1)),'bo');
    testo={['Nome curva =',indentation(i).name]};
    h1=text(max(indentation(i,1).inx(:,1))/3,
    max(indentation(i,1).iny(:,1))/1.2,testo);
%     pause
end

 %% FIT

% k=26e-9; %N/nm
for i=1:length(indentation)
    init_c=[-.1; -.1; 0.5 ];
        indice=find(indentation(i,1).inx<=-0.05); %<=-0.05
    options = optimset('LargeScale','on','MaxFunEvals',50000,
    'TolFun',1e-9,'TolX',1e-9);
    [c,resnorm,residual] = l
```

```
    sqcurvefit('FuncHertzModel',init_c,indentation(i,1).inx(indice),
    indentation(i,1).iny(indice),-3,-0.01,options);
    %     figure(i)
    h1=figure(4);
    h1=plot(indentation(i,1).inx,indentation(i,1).iny,'r.',
    indentation(i,1).inx(indice),
    FuncHertzModel(c,indentation(i,1).inx(indice)),'b-',
    'MarkerSize',10,'Linewidth',3);
    C(i,:)=c;
    Norm(i,1)=resnorm;
    indentation(i,1).moduloYoungin=C(i,3);
    init=c;
    testo={['Nome curva =',indentation(i).name];...
        ['Modulo di Young =',num2str(C(i,3)),' MPa'];...
        ['Isteresi=',num2str(indentation(i,1).isteresi),'pJ']};
    h1=text(max(indentation(i,1).inx(:,1))/3,
    max(indentation(i,1).iny(:,1))/1.2,testo);
    title('Curva IN');
%     pause
%     pause

end
```

Bibliography

[1] Maurice, D. M. In The eye. H. Davson. London, Academic Press, **1969**, INC. 1b.

[2] Ambekara R., Kimani C. Toussaint Jr., Amy Wagoner Johnsonb. *Jounal of the Mechanical Behavior of Biomedical Materials*. **2011**, 4, 223-236.

[3] Forrester J., Dick A., McMenamin P. and Roberts F. *The eye: basic sciences in practice*. Edinburgh, WB Saunders, **2002**.

[4] Hogan M., Alvarado J. and Weddel J. *Histology of the human eye*. Philadelphia, WB Saunders. **1971**.

[5] Iribarren R., Morgan, I., Nangia V., and Jonas, J. *Invest Ophthalmol Vis Sci*. **2011**, 53, 2, 543Ð550.

[6] Cowin, S.C. *Annu Rev Biomed Eng*. **2004**, 6, 77-107.

[7] Kadler, K.E.*Biochem J*. **1996**, 316, 1-11.

[8] Maroudas, A. Physical chemistry and the structure of cartilage. *J Physiol*. **1972**, 223, 1, 21-22.

[9] Beck and Brodsky, The collagen Triple-Helix, *Journal of structural biology*. **1988**,122, 1-2, 17-29.

[10] Canty, E.G. and K.E. Kadler. Procollagen trafficking, processing and fibrillogenesis. *J Cell Sci*. **2005**, 118, 7, 134-153.

[11] Hulmes, D. J. S. Building Collagen Molecules, Fibrils, and Suprafibrillar Structures, *J. Struct. Biol*. **2002**, 137, 2-10.

[12] Freund D. E., McCally R. L. and Farrell R. A. Effects of fibril orientations on light scattering in the cornea. *J Opt Soc Am A.* **1986** 3, 11, 1970-82.

[13] Edelhauser H., G. Smolin and R. Thoft. The cornea, Scientific foundations and clinical practice. *Brown and Company.* **1994**, 25-46.

[14] Xi Cheng and Peter M. Pinsky, J. R. Mechanisms of self-organization for the collagen fibril lattice in the human cornea. *Soc. Interface.* **2013**, 10, 512.

[15] Beems, E., and Van-Best, J. Light transmission of the cornea in whole human eyes. *Exp Eye Res.* **1990**, 50, 4, 393-395.

[16] Krachmer, J. H., Mannis, M. J., and Holland, E. J. Cornea: Fundamentals, Diagnosis and Management. *Elsevier MOSBY.* **2005**.

[17] Esheikh, A., Alhasso, D. and Rama, P. Assessment of the epitheliumÕs contribution to corneal biomechanics. *Exp Eye Res.* **2008**, 86, 445-451.

[18] Dubbelman M., Weeber H. A., van der Heijde R. G. and Volker-Dieben H. J. Radius and asphericity of the posterior corneal surface determined by corrected Scheimpflug photography. *Acta Ophthalmol Scand.* **2002**, 80, 4, 379-83.

[19] Zadnik K., Manny R. E., Yu J. A., Mitchell G. L., Cotter S. A., Quiralte J. C., Shipp M., Friedman N. E., Kleinstein R. N., Walker T. W., Jones L. A., Moeschberger M. L. and Mutti D. O. Collaborative Longitudinal Evaluation of Ethnicity and Refractive Study Group Ocular component data in schoolchildren as a function of age and gender. *Optom Vis Sci.* **2003**, 80, 3, 226-36.

[20] Saelens I. E., Bartels M. C. and Van Rij G. Manual trephination of mushroom keratoplasty in advanced keratoconus. *Cornea.* **2008**, 27, 650-655.

[21] Krachmer J. H., Feder R. S. and Belin M. W. Keratoconus and related noninflammatory corneal thinning disorders. *Surv Ophthalmol.* **1984**, 28, 293-322.

[22] Ucakhan O. O., Kanpolat A., Ylmaz N. and Ozkan M. In vivo confocal microscopy findings in keratoconus. *Eye Contact Lens.* **2006**, 32, 183-191.

[23] Rabinowitz Y., Wilson S. and Klyce S. Corneal Topography: Interpreting Videokeratography. New York , Tokyo. **1993**.

[24] Lee L., Hirst L. and Readshaw G. Clinical detection of unilateral keratoconus. *Aust N Z J Ophthalmol*. **1995**, 23, 129-133.

[25] Roy F.H., Fraunfelder F. W. and Fraunfelder F. T. Roy and FraunfelderÔs current ocular therapy. **2007**.

[26] Bawazeer A. M., Hodge W. G. and Lorimer B. Atopy and keratoconus: a multivariate analysis. *Br J Ophthalmol*. **2000**, 84: 834-836.

[27] Keares R. H. and Hoefle F. B. The contact lens correction of keratoconus. *Dabezies OH Jr, editor*. 1984. 1-55.

[28] Hashemi H. and Salari M. R. Intracorneal ring segment implantation for the management of keratoconus: safety and efficacy. *J Cataract Refract Surg*. **2007**, 33, 1886-1891.

[29] Hayes S., Kamma-Lorger C. S., Boote C., et al. The effect of riboflavin/UVA collagen cross-linking therapy on the structure and hydrodynamic behaviour of the ungulate and rabbit corneal stroma. *PLoS ONE*. **2013**, 8, 528-540.

[30] David P.S. O'Brart. Corneal collagen cross-linking: A review. *Journal of Optometry* **2014**, 7, 113-124.

[31] Botto's, K.M., Dreyfuss, J.L., Regatieri, C.V. et al (2008). Immunofluorescence confocal microscopy of porcine corneas following collagen cross-linking treatment with riboflavin and ultraviolet A. *J Refract Surg*. **2008**, 24, 7, 715-719.

[32] Wollensak G. Crosslinking treatment of progressive keratoconus: new hope. *Curr Opin Ophthalmol*. **2006**, 17, 356-360.

[33] Kanellopoulos, A.J. Collagen cross-linking in early keratoconus with riboflavin in a femtosecond laser-created pocket: initial clinical results. *J Refract Surg*. **2009**, 25, 11, 1034-1037.

[34] Bakke, E.F., Stojanovic, A., Chen, X. e Drolsum, L. Penetration of riboflavin and postoperative pain in corneal collagen crosslinking: excimer laser superficial versus mechanical full-thickness epithelial removal. *J Cataract Refract Surg*. **2009**, 35, 8, 1363-1366.

[35] Randleman, J.B., et al., Depth?dependent cohesive tensile strength in human donor corneas: implications for refractive surgery. *J Refract Surg*. **2008**. 24, 1, 85?9.

[36] Ethier C. and Simmons C. Introductory Biomechanics: From cells to organisms. *Cambridge University*. **2007**.

[37] Fung Y. C. Biomechanics: Mechanical Properties of Living TIssues. *Springer-Verlag*. **1981**.

[38] Sun, Y., Luo, Fertala. Direct quantification of the flexibility of type I collagen monomer. *Biochemical and Biophysical res*. **2002**, 295, 382-386.

[39] Hertz H., J. Reine Angew. Math. **1881**, 92, 156.

[40] Roa J. J., Oncins G., Diaz J., Sanz F. and Segarra M. Calculation of Young's Modulus Value by Means of AFM. *Recent Patents on Nanotechnology*. **2011**, 5, 27-36.

[41] Derjaguin, B.V., V.M. Muller, and Y.P. Toporov, Effect of contact deformations on the adhesion of particles. *Journal of Colloid and Interface Science*. **1975**, 53, 2, 314-326.

[42] Binnig G., Quate C.F., Gerber, C. Atomic Force Microscope. *Phys. Rev. Lett*. **1986**, 56, 9, 930-933.

[43] Hartmann, U. An Elementary Introduction to Atomic Force Microscopy and Related Methods. *Jul*. **2011**, 10.

[44] AlbrechtT. R., Akamine S., Carver T. E. , and Quate C. F. *Journal of Vacuum Science Technology*. **1990**, 8, 3386.

[45] Ziebarth, N.M., Wojcikiewicz, E.P., Manns, F., Moy, V.T., Parel, J.M., 2007. Atomic force microscopy measurements of lens elasticity in monkey eyes. Mol. Vis. 13, 504-510.

[46] Ziebarth, N.M., Arrieta, E., Feuer, W.J., Moy, V.T., Manns, F., Parel, J. Primate lens capsule elasticity assessed using atomic force microscopy. *Exp. Eye Res*. **2011**, 92, 490-494.

[47] Dias J. M., Noel M. Ziebarth. Anterior and posterior corneal stroma elasticity assessed using nanoindentation. *Experimental Eye Research*. **2013**, 115, 41-46.

[48] Burnham, N. A., Chen, X., Hodges, C. S., Matei, G. A., Thoreson, E. J., Roberts, C. J., Davies, M. C., Tendler, S. J. B. *Nanotechnology*. **2003**, 14,1-6.

[49] Cleveland, J. P., Manne, S., Bocek, D., Hansma, P. K. *Rev. Sci. Instrum.* **1993**, 64, 403-405.

[50] Hutter, J. L.; Bechhoefer, J. *Rev. Sci. Instrum.* **1993**, 64, 1868-1873.

[51] Gibson, C. T.; Watson, G. S.; Myhra, S. *Nanotechnology.* **1996**, 7, 259-262.

[52] Tortonese, M.; Kirk, M. Proc. *SPIE-.Int. Soc. Opt. Eng.* **1997**, 3009, 53-60.

[53] Bruker AFM Probes: Force Calibration Cantilevers. Support Note 013-000-000

[54] Chan E., Snibson G. R. Current status of corneal collagen cross-linking for keratoconus: a review. *Clin Exp Ophtalmol.* **2013**, 96, 155-164.

[55] Meek K. M., Hayes S. Corneal cross-linking. Review. *Ophthal Physl Opt.* **2013**, 33, 78-93.

[56] Spoerl E., Wollensak G., Seiler T. Increased resistance of crosslinked cornea against enzymatic digestion. *Curr Eye Res.* **2004**, 29, 35-40.

[57] Brummer G., Littlechild S., McCall S., Zhang Y., ConradGW. The role of nonenzymatic glycation and carbonyls in collagen crosslinking for the treatment of keratoconus. *Invest Ophth Vis Sci.* **2011**, 52, 6363-6369.

[58] Reiser K., McCormick R. J., Rucker R. B. Enzymatic and nonenzymatic cross-linking of collagen and elastin. *FASEB J.* **1992**, 6, 2439-2449.

[59] Zhang Y., Conrad A. H, Conrad G. W. Effects of ultraviolet-A and riboflavin on the interaction of collagen and proteoglycans during corneal cross-linking. *J Biol Chem.* **2011**, 286, 13011-13022.

[60] Kymionis G. D., Grentzelos M. A., Liakopoulos D. A., Paraskevopoulos T. A., Klados N. E., Tsoulnaras K. I., Kankariya V. P., Pallikaris I. G. Long-term Follow-up of Corneal Collagen Cross-linking for Keratoconus. *Cornea.* **2014**, 33, 1071-1079.

[61] Wollensak G, Iomdina E. Biomechanical and histological changes after corneal crosslinking with and without epithelial debridement. *J Cataract Refract.* **2009**, 35, 540-546.

[62] Scarcelli G., Kling S., Quijano E., Pineda R., Marcos S., Yun SH (2013) Brillouin microscopy of collagen crosslinking: noncontact depth-dependent analysis of corneal elastic modulus. *Invest Ophthalmol Vis Sci.* **2013**, 54, 1418-1425.

[63] Lombardo M., Serrao S., Rosati M., Ducoli P., Lombardo G. Biomechanical changes of the human cornea following transepithelial corneal cross-linking using iontophoresis. *J Cataract Surg.* **2014**, 40,10, 1706-1715.

[64] Dias J., Diakonis V. F., Kankariya V. P., Yoo S. H., Ziebarth N. M. Anterior and posterior corneal stroma elasticity after corneal collagen crosslinking treatment. *Exp Eye Res.* **2013** 116: 58-62.

[65] Lombardo M., Lombardo G., Carbone G., De Santo M. P., Barberi R., Serrao S. Biomechanics of the anterior human corneal tissue investigated with atomic force microscopy. *Invest Ophthalmol Vis Sci.* **2012**, 53, 1050-1057.

[66] Butt H. J., Cappella B., Kappl M. Force measurements with the atomic force microscope: tecnique, interpretation and applications. *Surf Sci Rep.* **2005**, 59, 1-152.

[67] Poggi M.A. (2005) A Method for Calculating the spring constant of atomic force microscopy cantilevers with a nonrectangular cross section. *Anal Chem.* **2005**, 77, 1192-1195.

[68] Last. Compliance profile of the human cornea as measured by atomic force microscopy. *Micron.* **2012** 43, 1293- 1298.

[69] Ruberti J.W., Roy A.S., Roberts C.J., Corneal Structure and Function. *Annu. Rev. Biomed. Eng.***2011**, 13, 269-295.

[70] Komai, Y. and T. Ushiki, The three?dimensional organization of collagen fibrils in the human cornea and sclera. *Invest Ophthalmol Vis Sci.* **1991**, 32(8): p. 2244?58.

[71] Levin L.A., Nilsson S.F.E., Ver Hoeve J., Wu S., Kaufman P.L., Alm A., AdlerÕs physiology of the eye, *Elsevier Health Sciences.* **2011**. ISBN: 0323057144, 9780323057141.